Assimilation of *GOES-16* ABI All-Sky Radiance Observations in RRFS Using EnVar: Methodology, System Development, and Impacts for a Severe Convective Event

SAMUEL K. DEGELIA,[a] XUGUANG WANG,[a] YONGMING WANG,[a] AND AARON JOHNSON[a]

[a] *School of Meteorology, University of Oklahoma, Norman, Oklahoma*

(Manuscript received 16 March 2023, in final form 6 July 2023, accepted 7 August 2023)

ABSTRACT: The Advanced Baseline Imager (ABI) aboard the *GOES-16* and *GOES-17* satellites provides high-resolution observations of cloud structures that could be highly beneficial for convective-scale DA. However, only clear-air radiance observations are typically assimilated at operational centers due to a variety of problems associated with cloudy radiance data. As such, many questions remain about how to best assimilate all-sky radiance data, especially when using hybrid DA systems such as EnVar wherein a nonlinear observation operator can lead to cost function gradient imbalance and slow minimization. Here, we develop new methods for assimilating all-sky radiance observations in EnVar using the novel Rapid Refresh Forecasting System (RRFS) that utilizes the Finite-Volume Cubed-Sphere (FV3) model. We first modify the EnVar solver by directly including brightness temperature (T_b) as a state variable. This modification improves the balance of the cost function gradient and speeds up minimization. Including T_b as a state variable also improves the model fit to observations and increases forecast skill compared to utilizing a standard state vector configuration. We also evaluate the impact of assimilating ABI all-sky radiances in RRFS for a severe convective event in the central Great Plains. Assimilating the radiance observations results in better spinup of a tornadic supercell. These data also aid in suppressing spurious convection by reducing the snow hydrometeor content near the tropopause and weakening spurious anvil clouds. The all-sky radiance observations pair well with reflectivity observations that remove primarily liquid hydrometeors (i.e., rain) closer to the surface. Additionally, the benefits of assimilating the ABI observations continue into the forecast period, especially for localized convective events.

KEYWORDS: Deep convection; Satellite observations; Data assimilation; Numerical weather prediction/forecasting

1. Introduction

Many modern weather satellites include high-resolution, passive imaging radiometers such as the Advanced Baseline Imager (ABI; Schmit et al. 2017) aboard *GOES-16* and *GOES-17* and the Advanced Himawari Imager (AHI; Chen et al. 2018) aboard *Himawari-8* and *Himawari-9*. These instruments provide detailed monitoring of a variety of meteorological phenomena including cloud structures and finer-scale convective features. The ABI and AHI also collect data as often as every ~30 s and with spatial resolutions of ~2 km for the infrared channels. Such high-resolution observations correspond well with the convective scale and could be particularly useful for high-resolution data assimilation (DA) and numerical weather prediction (NWP) forecasts. In cloudy regions, satellite radiance observations contain information about hydrometeors near cloud tops. These cloudy radiances are useful for observing developing clouds and pair well with radar reflectivity observations which only provide information about cloud hydrometeors after precipitation begins. Assimilating cloudy radiances can also aid in suppressing spurious clouds and are particularly useful for observing regions that are not typically monitored by conventional ground-based or upper-air observations. In cloud-free regions, infrared radiances contain information about mid- and upper-level thermodynamic properties. Assimilating clear-air data is also known to constrain midlevel waves (e.g., Johnson et al. 2022).

Recent studies explore the impacts of assimilating all-sky radiance observations for convection-allowing applications. Jones et al. (2020) assimilate all-sky radiances from the water vapor channels (6.2, 6.9, and 7.3 μm) aboard the ABI and find improved forecasts of convection, but also that cirrus clouds can become too expansive and degrade the thermodynamic fields. When using adaptive error inflation methods, Zhang et al. (2019) show improvements when assimilating ABI all-sky radiances that primarily result from suppressing spurious cloud cover. Recently, Johnson et al. (2022) develop adaptive observation error and additive inflation methods to improve the impacts of assimilating all-sky radiances. When applying these methods for a multisupercell event, they find that assimilating ABI all-sky radiances from mid and low-level water vapor channels results in better predictions for an upper-level shortwave trough, accelerated development of deep convective clouds, and increased strength of rotating updrafts. Chandramouli et al. (2022) further develop online, nonlinear bias correction methods using radar reflectivity as anchoring observations to separate model and observation biases when assimilating ABI data at the convective scale. This method further improves the impact of assimilating all-sky radiance observations by better suppressing spurious clouds and accelerating the development of existing cloud regions.

Each of the above studies that assimilate ABI all-sky observations for convective-scale NWP apply the ensemble Kalman filter (EnKF; Whitaker and Hamill 2002) method for DA. The EnKF is widely utilized for convection-allowing DA and NWP due to its ability to sample flow-dependent background error covariances and easily generate ensemble perturbations for the forecast period. However, hybrid DA approaches such as the ensemble variational (EnVar; Wang 2010) method are

Corresponding author: Samuel K. Degelia, sdegelia@ou.edu

DOI: 10.1175/MWR-D-23-0057.1

becoming increasingly popular in operational and research centers across the globe. These methods combine the benefits of the standalone EnKF with variational DA methods (see Wang 2010; Wang et al. 2013). The benefits of these hybrid systems compared to standalone systems (i.e., pure variational or pure EnKF) have been documented by many recent studies (e.g., Wang et al. 2007, 2008a,b; Barker et al. 2012; Wang et al. 2013; Pan et al. 2014; Lu et al. 2017; Wang and Wang 2017, 2021b).

Previous research of hybrid DA methods for the convective scale has primarily evaluated the impacts of assimilating radar reflectivity observations (e.g., Wang and Wang 2017; Gasperoni et al. 2023). Recently, Wang et al. (2022) assimilate all-sky water vapor radiances using EnVar and find some small advantages over assimilating clear-sky radiances for heavy rainfall accumulations. However, the Wang et al. (2022) study only features 9-km grid spacing and as such, no known studies evaluate the impacts of assimilating all-sky radiance observations using EnVar at convection-allowing resolutions. This research gap is primarily due to various complications that occur when assimilating observations with highly nonlinear forward operators such as those used for computing cloudy radiances. Strong nonlinearity associated with the forward operator can lead to imbalance in the gradient of the cost function which then can result in difficulties converging during minimization (Sun and Crook 1997). Similar problems have been documented when assimilating radar reflectivity observations in Wang and Wang (2017). As such, many questions remain about whether EnVar can be used successfully to assimilate ABI all-sky radiance observations.

As part of its shift to a Unified Forecast System (UFS), the National Oceanic and Atmospheric Administration (NOAA) recently began transitioning each of their NWP products to the Finite-Volume Cubed-Sphere (FV3; Lin 2004; Putman and Lin 2007; Harris et al. 2021) dynamical core. As part of this unified structure, NOAA's next generation convective-scale model and DA system will use FV3 in its limited area configuration (FV3-LAM; Black et al. 2021) and be known as the Rapid Refresh Forecasting System (RRFS; Alexander and Carley 2020). Given the benefits of hybrid systems detailed above, EnVar has been selected as the DA method for RRFS. Recently, Gasperoni et al. (2023) develop a fully cycled DA and forecast system based on the RRFS that features the assimilation of both conventional and convective-scale radar observations. This study further expands the RRFS system developed by Gasperoni et al. (2023) to include the assimilation of ABI all-sky radiance observations. We design methods to resolve the imbalance problem related to nonlinear observation operators and slow minimization associated with assimilating all-sky radiance observations. The impacts of these methods, and the impacts of assimilating ABI all-sky radiance observations in RRFS, are shown for a high-impact severe convective event from 26 to 27 May 2021.

The outline of this paper is as follows: section 2 presents a general overview of the RRFS DA and forecast system applied here. The ABI all-sky radiance observations, preprocessing methods, and case details are also discussed in this section. Section 3 introduces a method for directly including brightness temperature (T_b) as a state variable in EnVar to resolve the imbalance problem and accelerate convergence of the cost function. We also present impacts of applying this method for the 26–27 May convective event. Section 4 evaluates the impacts of assimilating ABI all-sky radiances alongside radar observations in the RRFS system. Finally, a summary of the results is found in section 5.

2. System configuration

a. *Overview of the FV3-LAM forecast and EnVar DA system*

We employ a fully cycled DA and forecast system designed to emulate the configuration of a future RRFS system following Gasperoni et al. (2023; Fig. 1a). The forecast model consists of FV3-LAM (Black et al. 2021; UFS Development Team 2022) and the DA component consists of 1) a Gridpoint Statistical Interpolation (GSI)-based EnVar used to update a control member and 2) a GSI-based EnKF used to update a 36-member ensemble. Given that we introduce a method of using T_b as a state variable to resolve an imbalance issue (see section 3), additional work is needed to develop static covariances for T_b if using the traditional hybrid configuration of EnVar. As such, as a first step to examine this method, we employ EnVar with only ensemble covariances (as in Gasperoni et al. 2023).

Prior to DA, we initialize the control member on a CONUS domain (Δx = 3 km; Fig. 1b) using the 0.25° analysis from the National Centers for Environmental Prediction (NCEP) Global Forecast System (GFS). The 36 ensemble members are configured on the same grid and use all the same settings. These members are initialized from the Global Ensemble Forecast System (GEFS; Wei et al. 2008) wherein members 1–30 are created using the GEFS analyses and members 31–36 are created using the first six members of the 6-h GEFS forecast initialized from the previous initialization time. Given that the GEFS forecasts are only output every 3 h, lateral boundary conditions (LBCs) for the hourly DA cycling period are instead generated using the same hourly GFS forecast for both the control member and each ensemble member (i.e., no perturbations are applied). During the forecast period, the LBCs are generated using the 3-h GEFS forecast for the ensemble members and the deterministic GFS for the control member. Additionally, we note that performing a 6-h spinup cycle prior to DA aids in the suppression of spurious convection that occurs in many ensemble members across the domain. We refer to Table 1 for a list of additional physics parameterizations and other configuration settings for FV3-LAM.

During DA, the background error covariances sampled from the 36-member ensemble are used to update the control member using EnVar; the ensemble members are correspondingly updated using EnKF (Fig. 1a). Conventional and storm-scale (i.e., radar reflectivity and ABI radiance) observations are assimilated separately due to the need to use observation-dependent localization radii (see Table 1 for specific values). These localization radii are selected by varying the values for the 26–27 May convective event and selecting those which produce the highest fractions skill score (FSS; Roberts and Lean 2008)

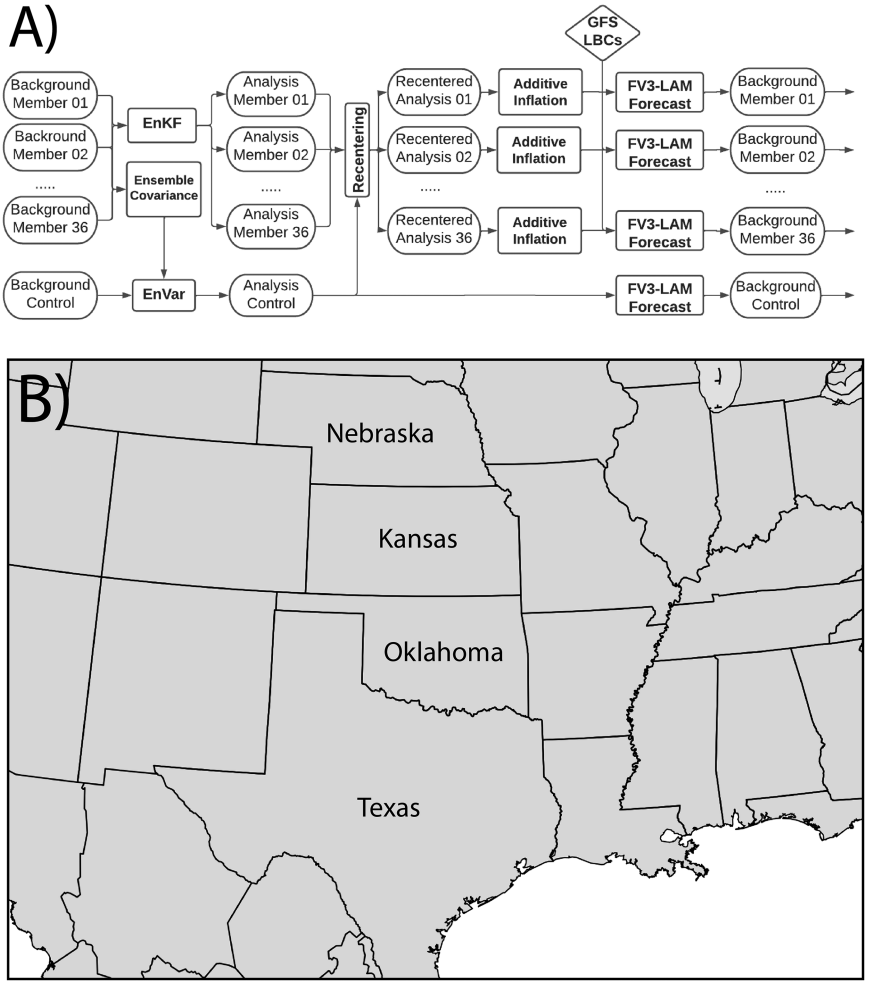

FIG. 1. System configuration for the RRFS-like system applied here including (a) a flowchart for the cycled DA system featuring a GSI-based EnVar, A GSI-based EnKF, and the FV3-LAM forecast component and (b) the model domain used for all DA cycling and forecast periods.

during the forecast period. After both observation sets are assimilated, the ensemble analyses are recentered around the control member to allow for two-way feedback following Wang et al. (2013). Two different types of covariance inflation are applied to maintain ensemble spread during cycled DA and to help spinup observed clouds in the model. These include the relaxation-to-prior-spread method (RTPS; Whitaker and Hamill 2012) and an additive inflation method (Johnson et al. 2022). These methods are described in detail below. We also refer to Table 1 for a list of additional DA parameters applied in this study.

RTPS is a multiplicative inflation method that inflates the ensemble analysis spread to some percentage of the original ensemble background spread as follows:

$$\sigma^a \leftarrow (1 - \alpha)\sigma^a + \alpha\sigma^b, \tag{1}$$

where σ^a and σ^b are the analysis and background ensemble standard deviation at each model grid point, respectively; and the parameter α defines the inflation magnitude. RTPS is commonly applied for many convective-scale DA studies (e.g., Harnisch and Keil 2015; Hu et al. 2019; Degelia et al. 2020; Gasperoni et al. 2020; Johnson et al. 2022) with large inflation magnitudes (i.e., $\alpha = 0.95$) being most common. Our initial experiments applied strong inflation to the analysis ensemble using $\alpha = 0.95$. However, these experiments produced large regions of spurious convection and cold cloud tops across the ensemble members, even when cloudy radiance observations were assimilated. Additionally, many ensemble members featured abnormally high analysis reflectivity (>80 dBZ) in regions where strong convection was observed. Experiments with varying values of α in Eq. (1) reveal that weaker inflation reduces the impact of this spurious precipitation and cloud cover, suggesting that optimal RTPS parameters are likely model sensitive and need to be tuned. We hypothesize that the additional spurious convection results from perturbations to cloud hydrometeors that are not fully removed during the EnKF. Instead, we find that an intermediate value ($\alpha = 0.30$) produces sufficient spread while also suppressing much of the

TABLE 1. List of FV3-LAM and DA settings used for all simulations.

Parameterization or DA setting	Scheme name or value	
Microphysical parameterization	Thompson et al. (2008)	
PBL parameterization	MYNN (Nakanishi and Niino 2006)	
Radiation parameterization (shortwave and longwave)	RRTMG (Iacono et al. 2008)	
LSM	RUC (Smirnova et al. 2016)	
Cumulus parameterization	None	
Model grid spacing (Δx, Δy)	3 km	
Grid dimensions	846 × 606	
Number of vertical levels	62	
Localization radii (conventional in situ observations)	Horizontal: 300 km	Vertical [$\ln(P/P_{ref})$]: 0.55 km
Localization radii (radar reflectivity, ABI all-sky radiances)	Horizontal: 15 km	Vertical [$\ln(P/P_{ref})$]: 2.2 km
Inflation factor (RTPS)	$\alpha = 0.30$	
Inflation factor (standard deviation for additive inflation)	0.25 K (temperature), 0.25 K (dewpoint temperature), and 0.25 m s^{-1} (wind)	

spurious convection. We note that these findings are not specific to assimilating radiance data and hold when only assimilating conventional and radar reflectivity observations. The experiments with $\alpha = 0.30$ also produce lower root-mean-square errors during cycled DA and higher skill during the forecast. As such, the set of experiments presented here apply RTPS inflation using $\alpha = 0.30$.

To better spin up cumulus clouds in the model, we further apply an additive inflation method to the analysis ensemble that is developed specifically for ABI all-sky radiances R (Johnson et al. 2022). This method randomly perturbs grid points that include clouds in the observations (observed cloud affect, $C_o > 2$ K) but are clear in the ensemble-mean background (forecast cloud affect, $C_f \leq 2$ K). The random perturbations are drawn from a Gaussian distribution with zero mean and a given standard deviation. The cloud affect properties are defined following Johnson et al. (2022) such that $C_f = \max\{0,\ T_b^{\lim} - T_b^f\}$ where T_b^f is the forecast brightness temperature and $T_b^{\lim}$ is the brightness temperature threshold between cloudy and clear sky determined by evaluating the distribution of T_b^f. We find that $T_b^{\lim} = 250$ K successfully delineates between clear and cloudy pixels. Likewise, the observed cloud effect is $C_o = \max\{0,\ T_b^{\lim} - (T_b^o - \text{bias})\}$ where T_b^o is the observed brightness temperature. Here, *bias* describes the average difference between T_b^f and T_b^o and is removed given that $T_b^{\lim}$ is determined using the background forecasts. We find that this additive inflation method improves simulated T_b and better spins up clouds during the early cycles when using standard perturbations of 0.25 K, 0.25 K, and 0.25 m s^{-1} for the temperature, dewpoint temperature, and wind fields below 500 hPa. These values follow those discussed in Johnson et al. (2022).

b. Observation and preprocessing methods

Observations assimilated here consist of conventional in situ, radar reflectivity, and ABI all-sky radiance observations. Conventional data are provided by the North American Mesoscale Data Assimilation System (NDAS; Rogers et al. 2009) and include surface, rawinsonde, aircraft, ship, and buoy observations. The radar reflectivity observations include the three-dimensional quality-controlled products produced in the Multi-Radar Multi-Sensor (MRMS; Zhang et al. 2016) dataset. Wang and Wang (2017) recently develop the capability to directly assimilate these radar observations in the GSI-based EnVar. Here, we reset reflectivity observations below 5 dBZ to 0 dBZ and assimilate them as clear air, while observations above 10 dBZ are assimilated as precipitation. We do not assimilate reflectivity observations between 5 and 10 dBZ given their ambiguity between meteorological and nonmeteorological echoes.

Finally, we also assimilate the channel-10 all-sky radiances collected by the ABI in the form of brightness temperature. The T_b for channel 10 is primarily sensitive to midlevel water vapor in clear air (weighting function peaks at ~625 hPa). Although other studies often assimilate multiple water vapor bands, Johnson et al. (2022) show that the channel-10 radiances are more impactful than the other water vapor bands for convection-allowing forecasts. As such, we elect to only assimilate a single band to more easily understand the impacts of applying the novel method in section 3. Version 2.3 of the Community Radiative Transfer Model (CRTM; Han et al. 2006) is used to compute the model priors for these radiance observations using each of the cloud hydrometeor species from the Thompson et al. (2008) microphysics scheme.

We apply a variety of preprocessing methods to the ABI all-sky radiances to optimize the impact of assimilating these data using EnVar. First, we remove partly cloudy observations given that their contributions to brightness temperature are ambiguous and either result from water vapor mixing ratio (as in clear air) or cloud hydrometeors (as for cloudy observations). Unlike Johnson et al. (2022) who remove partly cloudy pixels using a cloud fraction product, we instead apply a standard deviation threshold to the ABI channel-2 reflectance observations similar to Saunders and Kriebel (1988). The channel-2 observations are collected at a much higher spatial resolution (0.5 versus 2 km for channel-10 radiances) and thus contain information about "subgrid" cloud structures within the channel-10 observations. We remove any channel-10 observations where the corresponding standard deviation of the channel-2 reflectance is greater than 0.05 over a ±2-pixel window. This method removes only a small number of observations (~5% of the total dataset) located primarily near the edges of larger cloud structures.

After removing any partly cloudy pixels, we further thin the ABI observations to 4-km resolution primarily to limit the impacts of correlated observation errors common for satellite datasets (i.e., Weston et al. 2014; Bathmann and Collard 2020). Thinning can also potentially limit impacts of dry biases when assimilating clear-air radiance observations (e.g., Jones et al. 2020; Zhu et al. 2023). We also apply a parallax correction (Wang and Huang 2014; Jones et al. 2020; Johnson et al. 2022) to account for potential location errors for cloudy observations caused by the viewing angle of the satellite. Unlike Johnson et al. (2022), we do not apply bias correction or any adaptive observation error methods for the channel-10 all-sky radiances. We evaluate the impacts of these methods for the 26–27 May case using the RRFS system and find decreased impacts for nearly all verification metrics. Instead, we set the observation errors for ABI radiances to a constant 3 K following Minamide and Zhang (2017). We plan to develop flow-dependent observation errors and bias correction methods for EnVar in a future study.

Finally, Johnson et al. (2022) also discuss disabling innovation checks when assimilating ABI radiances given that observation departures are expected to be very large when assimilating all-sky data. This typically occurs when one of either the model or observations features clear air while the other features a cloud. When assimilating ABI radiances in EnVar, we sometimes find that spuriously large reflectivity (>100 dBZ) can develop in the analyses when the innovation is very large, such as when assimilating clear-air radiances in the presence of spurious clouds. We find that these spurious reflectivity values result from a positive correlation between the cloud hydrometeors and brightness temperature above the tropopause. Given that temperature increases with height above the tropopause, ensemble members with stronger overshooting tops would also feature warmer brightness temperatures. As such, assimilating clear-air observations in these regions can sometimes result in increased cloud hydrometeor content in the upper troposphere. To resolve this problem, we elect to enable innovation checks only in the presence of overshooting tops. Here, we determine overshooting tops by comparing the tropopause height in pressure (p_{trop}) to the peak of the weighting function for channel-10 radiances (p_{weight}). Any observations are removed if their innovation is greater than +50 K (i.e., clear-air observation but simulated deep convection) and if $p_{\text{weight}} < p_{\text{trop}}$. This modification to the methods in Johnson et al. (2022) entirely remove the anomalously large reflectivity values in the analysis and leads to small increases in skill throughout the subsequent forecast period.

c. Case details and experiment design

We evaluate novel methods for assimilating ABI all-sky radiances in EnVar for a severe convective event on 26–27 May 2021. The single case study allows us to better understand how these methods modify specific convective features and to track those changes throughout the forecast period. This case featured isolated convection that developed along a warm front in northwest Kansas between 1500 and 1800 UTC 26 May (Fig. 2a). The early convection later strengthened into a supercell at 2000 UTC and produced a tornado (circled region of convection in Fig. 2c). Observed radiances at this time reveal a circular anvil cloud associated with the supercell with cloud top temperatures cooling to 205 K (Fig. 2d). More widespread convection developed later ahead of a lee trough and dryline, later growing upscale into a series of weakly organized, mesoscale convective systems (MCSs) in Nebraska (Fig. 2e). Eventually, the original supercell weakened and began to dissipate by 0600 UTC 27 May (Fig. 2g). The secondary convection in Nebraska then propagated southeastward into northern Kansas, producing severe wind and hail reports by 0600 UTC (Fig. 2g). The anvil clouds associated with these MCSs began to merge, leading to a large region of cold cloud tops (Fig. 2h).

We refer to Fig. 1a for an example diagram of one DA cycle. Each experiment consists of seven hourly cycles that are first performed at 1800 UTC following a 6-h spinup period. We note that while hourly cycling is performed here to be consistent with the goals of RRFS, various studies find that subhourly DA can lead to additional benefits when assimilating radar (e.g., Yang and Wang 2023) and all-sky radiances (e.g., Honda et al. 2018; Zhang et al. 2021). Here, the DA period continues until 0000 UTC 27 May after which a 12-h forecast is initialized from the control member analysis and the first ten ensemble members. This cycling configuration is applied for a total of four experiments (Table 2). These include three observation impact experiments to determine the impact of assimilating ABI all-sky radiances in a RRFS-like system (NORADAR, RADAR, and RADAR+ABI). One experiment is also conducted to evaluate the impact of including brightness temperature as a state variable (RADAR+ABI_NOTBSTATE; section 3).

3. Addition of T_b as a state variable in GSI-based EnVar

a. Minimization problems when assimilating T_b in EnVar

Wang (2010) defines the gradient of the cost function, J, for EnVar as

$$\nabla_{\mathbf{a}} J = \mathbf{A}^{-1}\mathbf{a} + \mathbf{D}^{\mathrm{T}}\mathbf{H}^{\mathrm{T}}\mathbf{R}^{-1}(\mathbf{H}\mathbf{x}' - \mathbf{y}^{o\prime}), \tag{2}$$

where $\mathbf{a}$ indicates the extended control vector, $\mathbf{A}$ is a block-diagonal matrix consisting of the localization applied to the ensemble covariance, $\mathbf{x}'$ is the analysis increment, $\mathbf{R}$ is the observation error covariance matrix $\mathbf{H}$ is the linearized observation operator, and $\mathbf{y}^{o\prime}$ is the innovation vector. The matrix $\mathbf{D}$ is defined as $[\mathrm{diag}(\mathbf{x}_1^e)\ldots\ \mathrm{diag}(\mathbf{x}_k^e)]$ where $\mathbf{x}_k^e$ represents the kth ensemble perturbation normalized by $\sqrt{K-1}$. Here, K represents the ensemble size. The state variables used in this system include zonal and meridional wind, vertical velocity, virtual and sensible temperature, three-dimensional and surface pressure, Q_{vapor}, Q_{rain}, Q_{liquid}, Q_{snow}, Q_{ice}, Q_{graupel}, reflectivity, and channel-10 brightness temperature (only for RADAR+ABI). During minimization, $\mathbf{H}\mathbf{x}'$ is iterated upon following methods in Derber and Rosati (1989) and Wu et al. (2002) to find the optimal analysis increment $\mathbf{x}'$.

Initial attempts to assimilate ABI all-sky radiances in the RRFS and EnVar system resulted in very long convergence times for the described configuration (>3000 iterations and >2 h of processing time before convergence; Fig. 3a). Conversely, when assimilating only radar reflectivity, $\mathbf{x}'$ converges within only

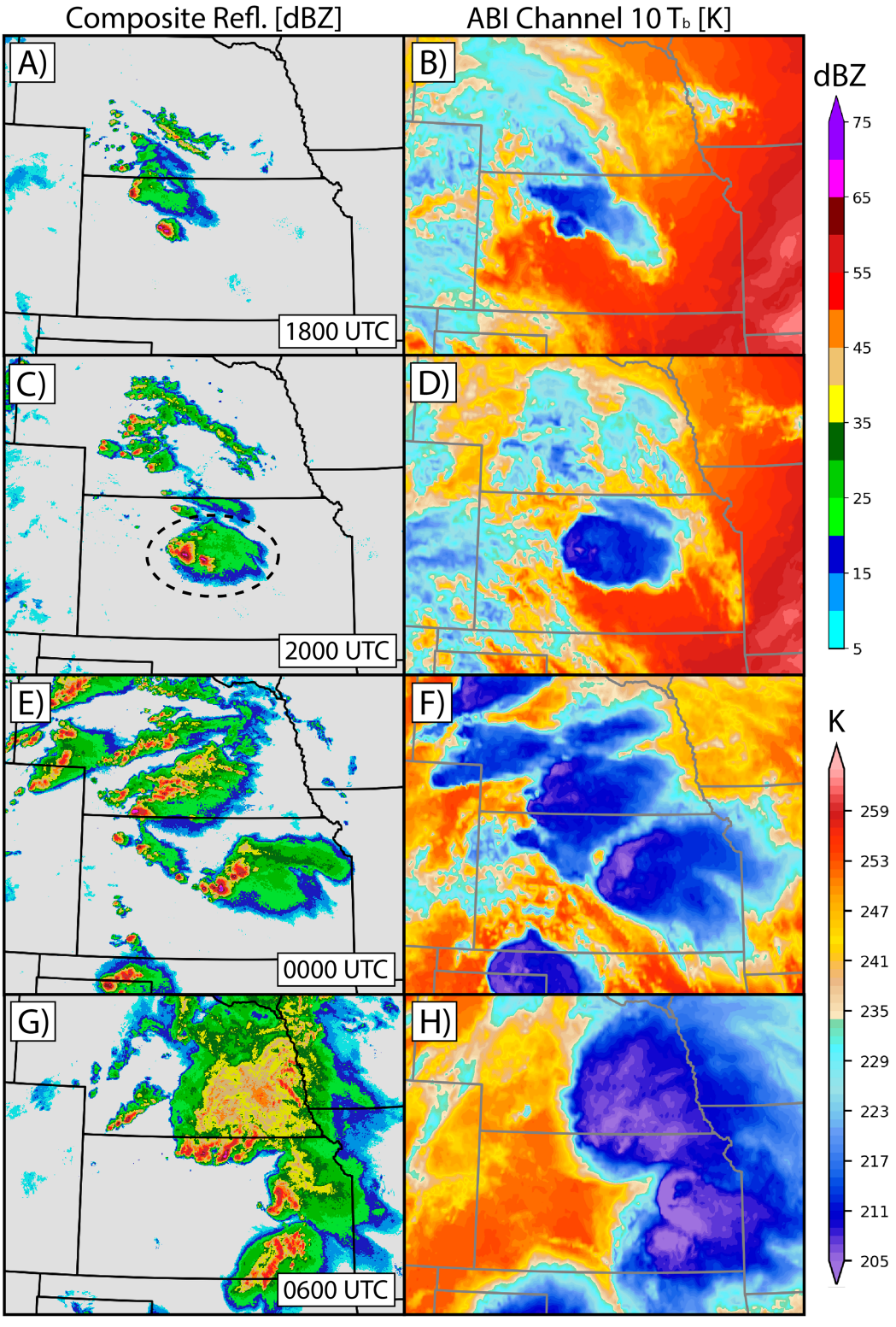

FIG. 2. Evolution of observed (a),(c),(e),(g) composite reflectivity (dBZ) and (b),(d),(e),(f),(h) ABI channel-10 brightness temperature (K) for the 26–27 May tornadic supercell in Kansas.

TABLE 2. List of experiments.

Experiment	Observations assimilated	Other parameter changes
NORADAR	Only conventional in situ observations	—
RADAR	Conventional in situ and radar reflectivity observations	—
RADAR+ABI	As in RADAR but also with assimilating channel-10 all-sky radiance observations	—
RADAR+ABI_NOTBSTATE	As in RADAR+ABI	Not including T_b as a state variable

~50 inner loop iterations. Upon further inspection, we find that the ABI radiances likely lead to a cost function gradient ($\nabla_{\mathbf{x}} J$) that is highly imbalanced between cloud hydrometeors and other state variables. Sun and Crook (1997) demonstrate how cost function gradient imbalance can prevent convergence in 4DVar, and Wang and Wang (2017) illustrate related problems when assimilating reflectivity observations in GSI-based EnVar. Figure 4 shows $\mathbf{H}^{\mathrm{T}}$, also referred to as the Jacobian, in Eq. (2) for an example clear-air observation assimilated with spurious deep convection present in the model prior; $\mathbf{H}^{\mathrm{T}}$ relates changes in brightness temperature T_b to changes in the state variables and is computed by CRTM when assimilating satellite radiance observations in GSI. For the example observation, $\mathbf{H}^{\mathrm{T}}$ differs by multiple orders of magnitude for each state variable. For cloud hydrometeors (e.g., Q_{rain} shown in Fig. 4c), $\mathbf{H}^{\mathrm{T}}$ can often be extremely large, especially when deep convection is present. These large differences in $\mathbf{H}^{\mathrm{T}}$ can thus result in Eq. (2) becoming

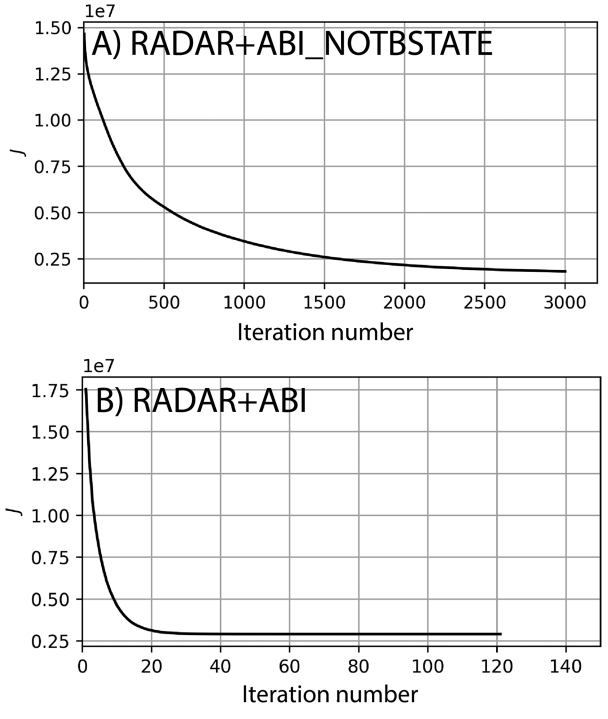

FIG. 3. Cost function values for each iteration when assimilating only ABI observations. (a) The default state vector is included without T_b and (b) T_b is included as a state variable following the description in section 3a.

imbalanced for different state variables. This theory is further supported by the differences in $\mathbf{H}^{\mathrm{T}}$ being larger for cloud hydrometeors, and convergence correspondingly slower, when more convection is active in the domain (not shown).

To resolve the imbalance issue, we elect a similar solution to that described in Wang and Wang (2017) who directly assimilate radar observations by introducing reflectivity (dBZ) as a state variable. Wang and Wang (2017) show that this method can reduce imbalance and improve probabilistic forecasts of low-level vorticity and persistence of a midlevel mesocyclone. Here, we extend the state vector in GSI to directly include T_b as a state variable. This modification results in $\mathbf{H}^{\mathrm{T}}$ being reduced to an identity matrix when assimilating T_b. We note that this method requires T_b to be computed for each ensemble member, for example in $\mathbf{D}^{\mathrm{T}}$, in model space. To accomplish this, we add a standalone step prior to DA wherein CRTM is called on a set of observations interpolated onto the model grid such that GSI can subsequently output the ensemble priors of T_b. These priors $\mathbf{x}_k$ are then appended to the typical FV3-LAM output files before being treated as a state variable during the subsequent DA step.

Finally, this method also requires further modifications to the EnVar solver in GSI to account for T_b being a two-dimensional state variable while other variables are three-dimensional. In GSI, $\mathbf{x}'$ is computed in Eq. (2) as follows:

$$\mathbf{x}' = \sum_{k=1}^{K} (\mathbf{a}_k \circ \mathbf{x}_k^e), \tag{3}$$

where $\mathbf{a}_k$ is the unitless control variable for the kth ensemble member. However, GSI computes only a single, three-dimensional, $\mathbf{a}_k$ that is the same for each state variable. To compute $\mathbf{x}'$ for two-dimensional variables, a single level of $\mathbf{a}_k$ can be selected that corresponds to the observation level (e.g., the lowest model level of $\mathbf{a}_k$ when including surface pressure as a state variable). This method is consistent with the original derivation of $\mathbf{a}_k$ presented in Wang (2010). For our extension that includes T_b as a state variable, we modify Eq. (3) to select the level of $\mathbf{a}_k$ that is closest to the peak of the weighting function computed in GSI. We note that GSI computes the peak of the weighting function by determining the level where the transmittance output by CRTM is changing the fastest.

b. *DA and forecast impacts when including T_b as a state variable*

Extending the state vector to include T_b largely solves the imbalance issue given that $\mathbf{H}^{\mathrm{T}}$ reduces to an identity matrix.

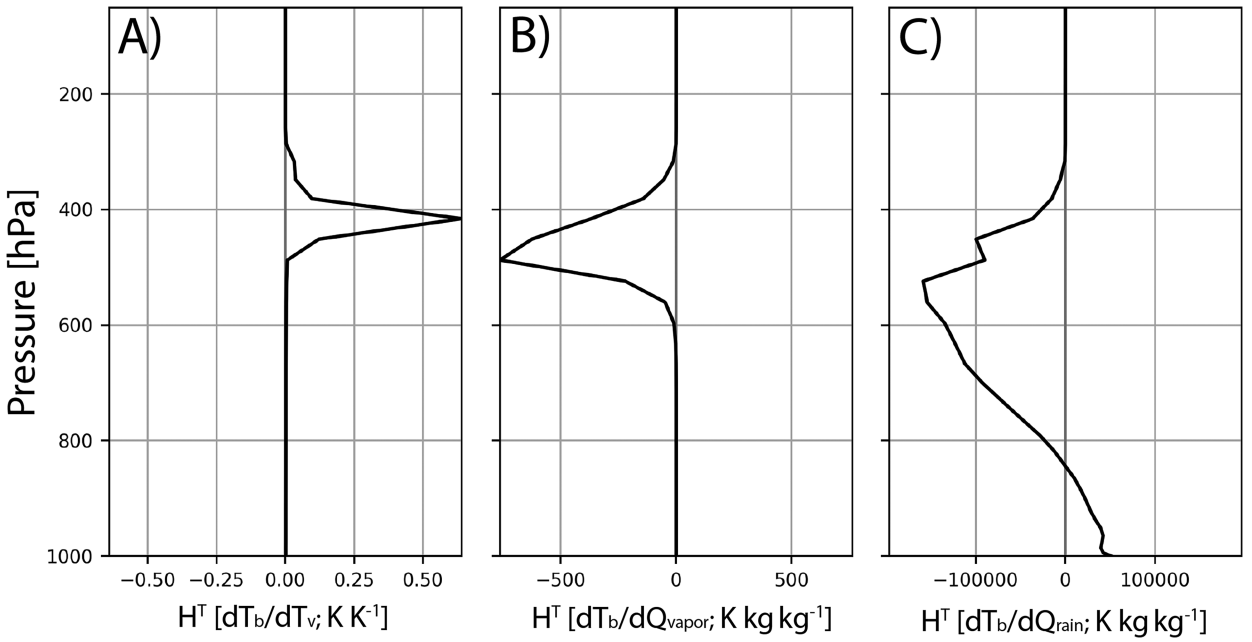

FIG. 4. Profiles of $\mathbf{H}^{\mathrm{T}}$ for a clear-air T_b observation assimilated within simulated deep convection. Shown are profiles for (a) virtual temperature (K K^{-1}), (b) water vapor mixing ratio (K kg kg^{-1}), and (c) rainwater mixing ratio (K kg kg^{-1}).

Given the improved balance, the addition of T_b as a state variable also correspondingly resolves the slow minimization problem. For the first DA cycle, RADAR+ABI_NOTBSTATE requires upward of ~3000 iterations to converge on a solution (Fig. 3a). However, the modification in RADAR+ABI converges in only ~40 iterations (Fig. 3b). These minimization times are much more realistic for operational settings and are closer to those seen when only assimilating conventional in situ and/or radar reflectivity observations. This result also parallels the findings from Wang and Wang (2017) when assimilating radar reflectivity observations.

We also compare DA and forecast impacts for the 26 May case when assimilating ABI all-sky radiances with and without T_b as a state variable (Figs. 5–7). We find large reductions in root-mean-square reflectivity errors (Fig. 5a) beginning at the second cycle and similar error reductions for simulated T_b

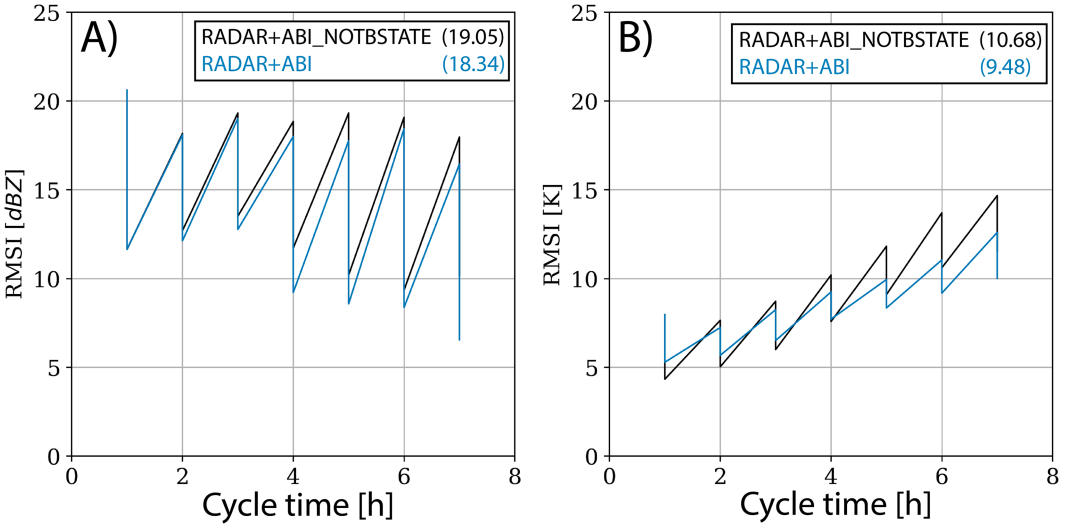

FIG. 5. Root-mean-square innovation (RMSI) during each DA cycle for (a) composite reflectivity (dBZ) and (b) simulated brightness temperature (K). The annotations in the legend represent the cycle-averaged RMSI for only the background cycles. Shown is a comparison between assimilating radiance observations using the default state vector without T_b and the extended state vector including T_b.

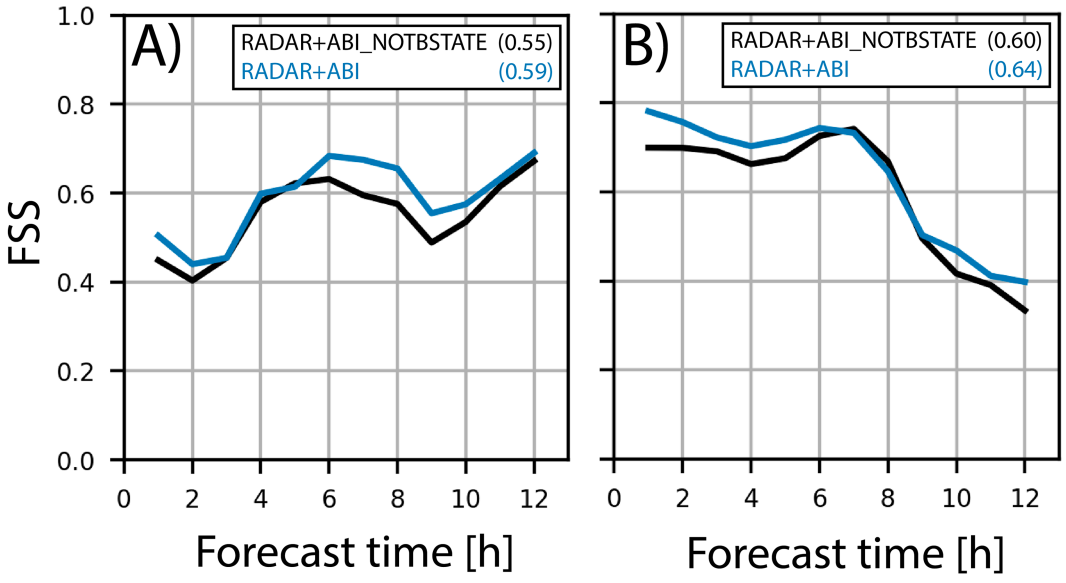

FIG. 6. Fractions skill score (FSS) during the forecast period for (a) composite reflectivity (dBZ) and (b) simulated brightness temperature (K). The annotations in the legend represent the forecast-averaged FSS. The figures are computed using a 15-km neighborhood and with thresholds of (a) 30 dBZ and (b) 230 K.

beginning at the fourth cycle (Fig. 5b). Overall, including T_b as a state variable reduces the mean error by 0.71 dBZ and 1.20 K when averaged over each of the background cycles. This result suggests that even with 3000 iterations, the original RADAR+ABI_NOTBSTATE experiment does not fully converge and correctly fit the reflectivity and brightness temperature observations.

The benefits of this method continue into the forecast period on 27 May (Fig. 6). During the forecast, little improvements are seen for the supercell and MCSs of interest discussed in later sections (not shown). Instead, most of the impacts relate to additional reductions of spurious convection and cloud cover. We note that the increase in reflectivity skill after forecast hour 3 (Fig. 6a) likely corresponds to the growth of the discrete convection over Kansas and Nebraska into an MCS that is better simulated in all experiments (see section 4c). The FSS in Fig. 6b is computed with a threshold of 230 K which we find to sufficiently separate convective clouds from nonconvective clouds (see Fig. 2). Including T_b as a state variable leads to a small increase in skill for reflectivity, with the largest improvements during the 6–10-h forecast period when convection is strongest (Fig. 6a). Conversely, the improvements to the T_b forecast are, while still positive, weakest during the 6–10-h forecast period (Fig. 6b) as the anvil clouds grow large and cover most of the forecast region.

Examples of the reduction of spurious convection and cloud cover when using T_b as a state variable are shown in Fig. 7. To be consistent between RADAR+ABI_NOTBSTATE and RADAR+ABI, we note that the simulated T_b in Fig. 7 and all subsequent figures is plotted by rerunning GSI and CRTM using the analyzed cloud hydrometeor and thermodynamic fields (as opposed to plotting T_b directly analyzed by EnVar). Both experiments generally simulate large regions of spurious convection and cloud cover in parts of southern and eastern Texas (Figs. 7a–c). Additional spurious convection is simulated in parts of western Kansas and along the Kansas–Oklahoma border (see southern circled region in Figs. 7a–c). However, including T_b as a state variable in the RADAR+ABI experiment removes large amounts of this spurious precipitation and better matches observed reflectivity and brightness temperature fields (Figs. 7c,f). Many of the spurious anvil clouds in eastern Texas are also removed in RADAR+ABI compared to RADAR+ABI_NOTBSTATE (circles in Figs. 7e,f).

4. Observation impacts for 26 May severe convective event

In this final section of results, we demonstrate the observation impacts when assimilating ABI all-sky radiances in a RRFS system using GSI-based EnVar. We compare three experiments listed in Table 2 including NORADAR, RADAR, and RADAR+ABI. The RADAR+ABI experiment included here includes the addition of T_b as a state variable along with the various developments discussed in section 2.

Quantitative verification metrics are first shown for these observation impact experiments in Fig. 8. Assimilating ABI all-sky radiance observations in RRFS shows small but consistent improvements to both the background and analysis RMSI for reflectivity (~1-dBZ error reduction; Fig. 8a). These impacts are much smaller than the benefits gained from assimilating reflectivity observations (~3-dBZ error reduction for background forecasts). We note that the reflectivity verification in Fig. 8 is only computed over grid points with observed reflectivity greater than 20 dBZ (i.e., verification does not represent impacts to spurious precipitation). However, the impacts to the simulated T_b fields (Fig. 8b), which do account for the removal of spurious clouds, are much larger and are similar to the

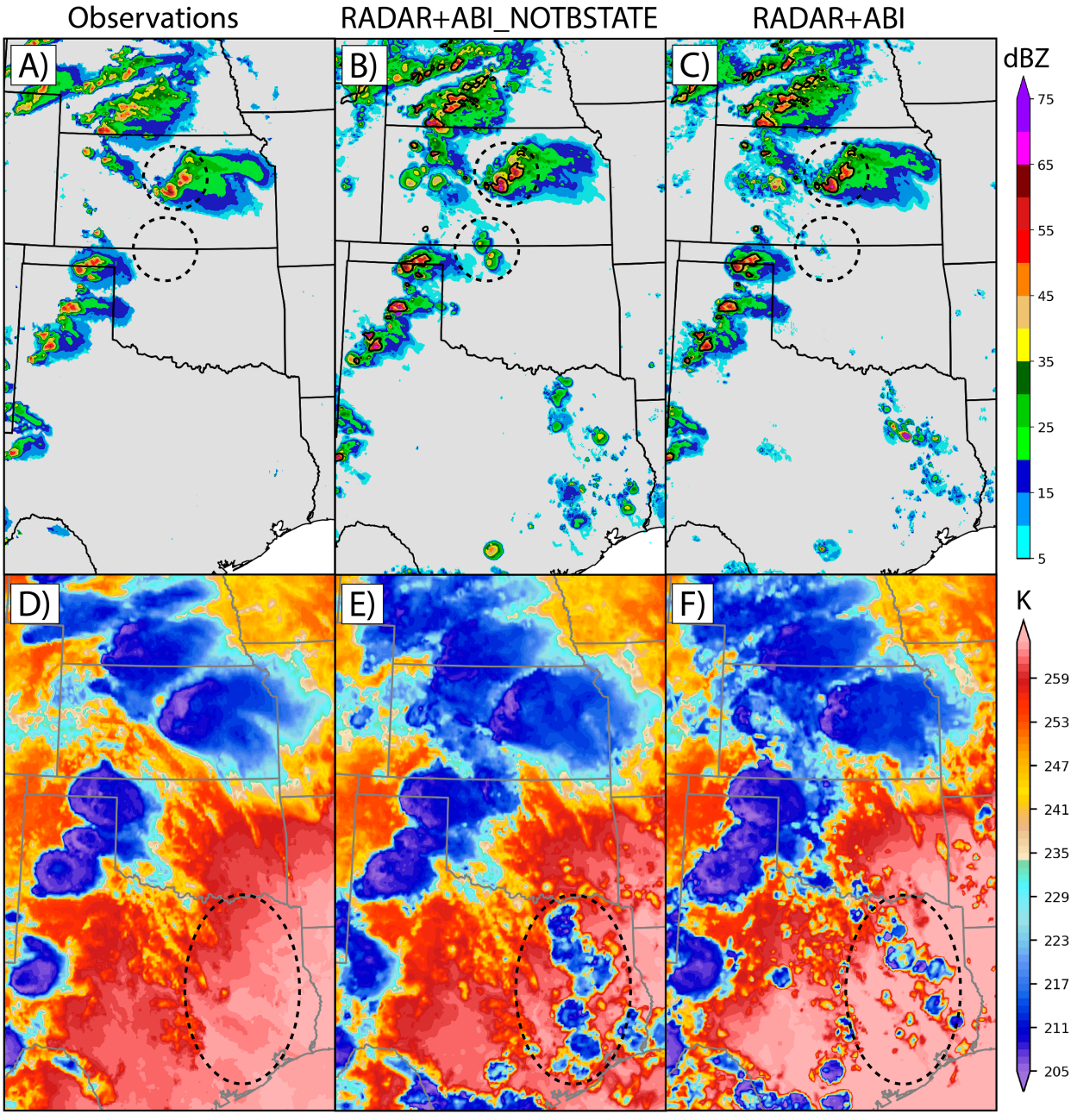

FIG. 7. Simulated (a)–(c) composite reflectivity (dBZ) and (d)–(f) brightness temperature (K) valid during the final DA cycle at 0000 UTC 27 May. (a),(d) Observations and a comparison between assimilating radiance observations using (b),(e) the default state vector without T_b and (c),(f) the extended state vector including T_b. Overlaid in solid black contours in (a)–(c) are observed composite reflectivity greater than 30 dBZ.

magnitude of improvements gained from assimilating reflectivity observations. Each cycle of RADAR+ABI reduces the T_b errors by ~3 K compared to the corresponding background errors. The final background errors for T_b are also reduced by ~3 K compared to RADAR and ~7 K compared to NORADAR. This result indicates that significant benefits to the cloud structures and overall mesoscale environment can be gained when assimilating ABI all-sky radiances in addition to radar observations. Similar findings were recently reported by Eure et al. (2023) using a GSI-based EnKF. While not shown here, we find that the impacts to RMSI for brightness temperature (Fig. 8b) are larger when adding observed convective or stratiform clouds compared to removing spurious clouds (though the latter impacts are still large and positive). Examples of individual benefits are shown in subsequent sections.

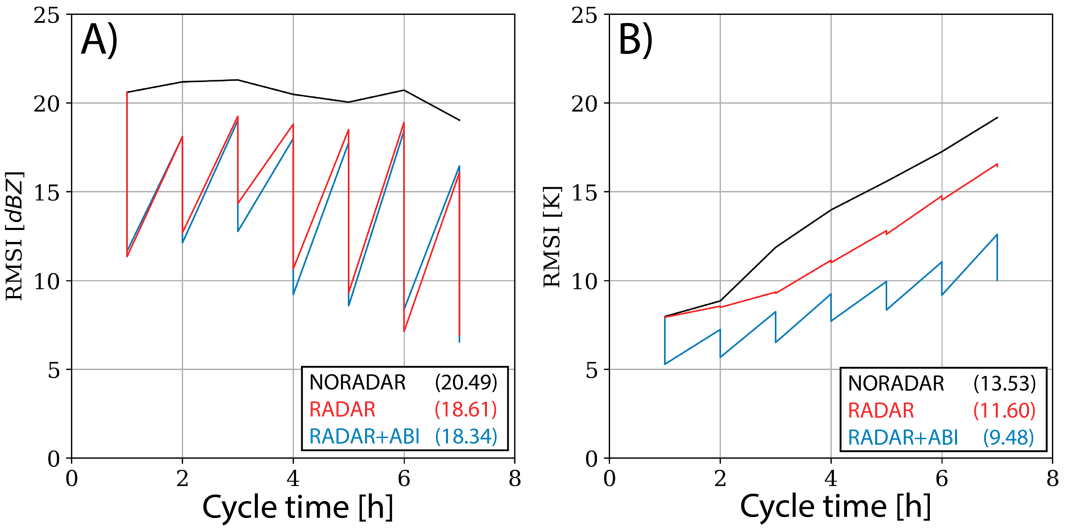

FIG. 8. As in Fig. 5, but for the observation impact experiments.

a. *Impacts for Kansas supercell*

Assimilating the ABI all-sky radiances produces large improvements in the analysis and background forecasts for the tornadic supercell in central Kansas (Figs. 9 and 10). Despite directly assimilating reflectivity observations, the RADAR experiment does not correctly analyze the convective core of the supercell until the fourth DA cycle at 2100 UTC (Fig. 9k). Additionally, neither the weaker precipitation downstream of the strongest convection (Figs. 9j,l), nor the widespread anvil cloud (Figs. 10j,l), are analyzed at this time. While not shown here, the background forecasts take an extra hour (2200 UTC) to maintain the deep convection on its own. The poor analysis of the storm likely results from a lack of spread in the ensemble given that no ensemble members correctly simulate the convection. This spinup problem could likely be at least partially resolved by including some portion of static covariances in EnVar instead of using the fully ensemble configuration applied here (i.e., Wang and Wang 2021a).

Conversely, when assimilating the ABI all-sky radiances together with the radar reflectivity observations, RADAR+ABI begins to introduce cloud hydrometeors by the first DA cycle (Fig. 10c) and correctly analyzes the supercell as early as the second DA cycle at 1900 UTC (Fig. 9f). The downstream precipitation and anvil cloud are also correctly analyzed and closely match the observations by 2000 UTC (Figs. 9g,i and 10g,i). We hypothesize that the improved analysis primarily results from the ABI observations adding hydrometeors associated with the anvil cloud and supporting larger spread for precipitating hydrometeors. Overall, assimilating the ABI all-sky radiances complements the radar reflectivity observations and results in improved spin up time for the supercell by 2–3 h. Additionally, without assimilating the cloudy radiances (which are often ignored), the convective-scale benefits of assimilating the radiance observations would be much smaller.

b. *Impacts for spurious convection*

FV3-LAM and RRFS systems are currently known to overpredict convection such that forecasts often feature many spurious cells that are too strong and widespread (e.g., Wicker et al. 2020). This at least partially results from updrafts for simulated convection being too strong and tall compared to observations, leading to many widespread spurious anvil clouds (Johnson et al. 2023). Improving methods to suppress this convection, including its environmental impacts, remains a top priority before these systems are used in an operational setting.

Many studies document the ability for clear-air radar reflectivity observations to suppress spurious convection in convection-allowing NWP models (e.g., Tong and Xue 2005; Aksoy et al. 2009; Degelia et al. 2018; Duda et al. 2019). However, without very large vertical localization radii that could degrade other fields, assimilating these clear-air observations typically only suppresses precipitating hydrometeors and can have little impact on cloud hydrometeors aloft. As such, the environmental impacts of the spurious convection often linger, including remnant anvil clouds that could inhibit insolation and prevent the development of future convection in these regions (Oberthaler and Markowski 2013). We find such impacts when assimilating radar reflectivity observations for the 26 May case (Figs. 11b,d). We note that all the simulated convection and clouds shown in Figs. 11 and 12 is spurious and not observed. Assimilating radar reflectivity observations removes or weakens most of the spurious precipitation in Texas compared to the background forecast (Figs. 11b,d). These improvements are primarily related to the removal of rain hydrometeors below 600 hPa (Fig. 13b). However, the simulated anvil clouds associated with this precipitation still remains in the analysis for RADAR (Figs. 12b,d). The spurious clouds simulated in RADAR are primarily associated with snow hydrometeors that are not fully suppressed near the tropopause (Fig. 13c).

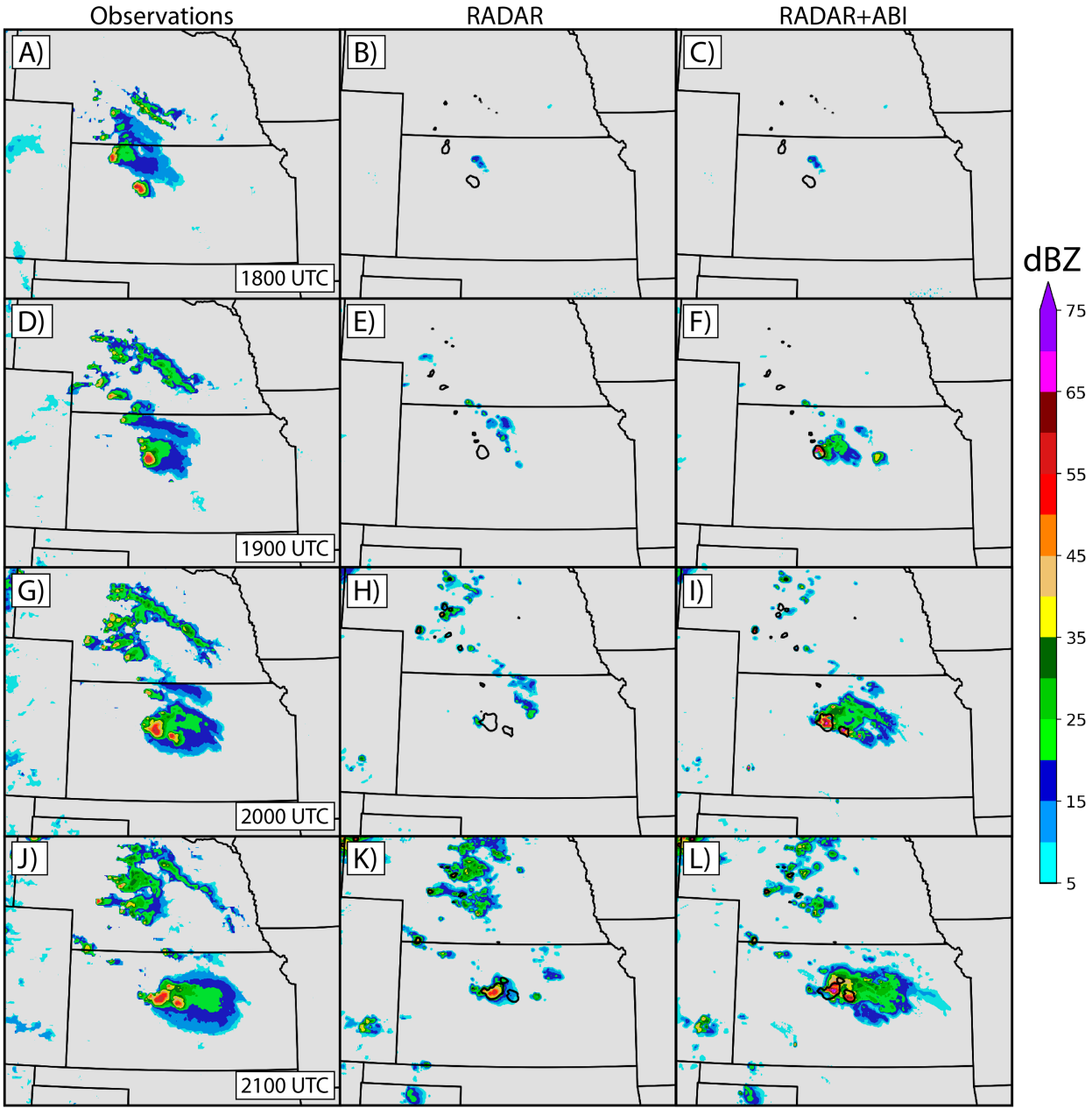

FIG. 9. Observations and analyses of composite reflectivity (dB*Z*) for the tornadic supercell during each DA cycle between 1800 and 2100 UTC 26 May. (left) Observations, (center) analyses for the RADAR experiment, and (right) analyses for the RADAR+ABI experiment. Overlaid in solid black contours for the center and right columns are observed composite reflectivity greater than 30 dB*Z*.

Assimilating radiance observations using ensemble-based DA methods can improve such problems (Koenig and de Coning 2009) given the correlation between cloud-top temperature and ice hydrometeors (e.g., Zhang et al. 2021). While the reflectivity analysis in RADAR+ABI features similar suppression of the spurious reflectivity echoes in eastern Texas (Figs. 11c,e), the brightness temperature in RADAR+ABI is greatly improved compared to RADAR (Fig. 12). Simulated cloud-top temperatures are increased by ~20 K compared to the background, primarily due to negative increments (i.e., removal) of snow hydrometeors near the top of the tropopause that is much larger in RADAR+ABI compared to RADAR (Fig. 13c). As such, assimilating the ABI radiance observations complements the radar reflectivity observations by removing hydrometeors near the tropopause. We refer to this suppression of spurious convection by radiance observations as "top-down suppression."

Despite being partially removed, we note that the spurious anvil clouds in eastern Texas are still present in the RADAR+ABI analysis (Fig. 12e) while the corresponding reflectivity echoes are almost entirely removed (Fig. 11e). The analysis increments to

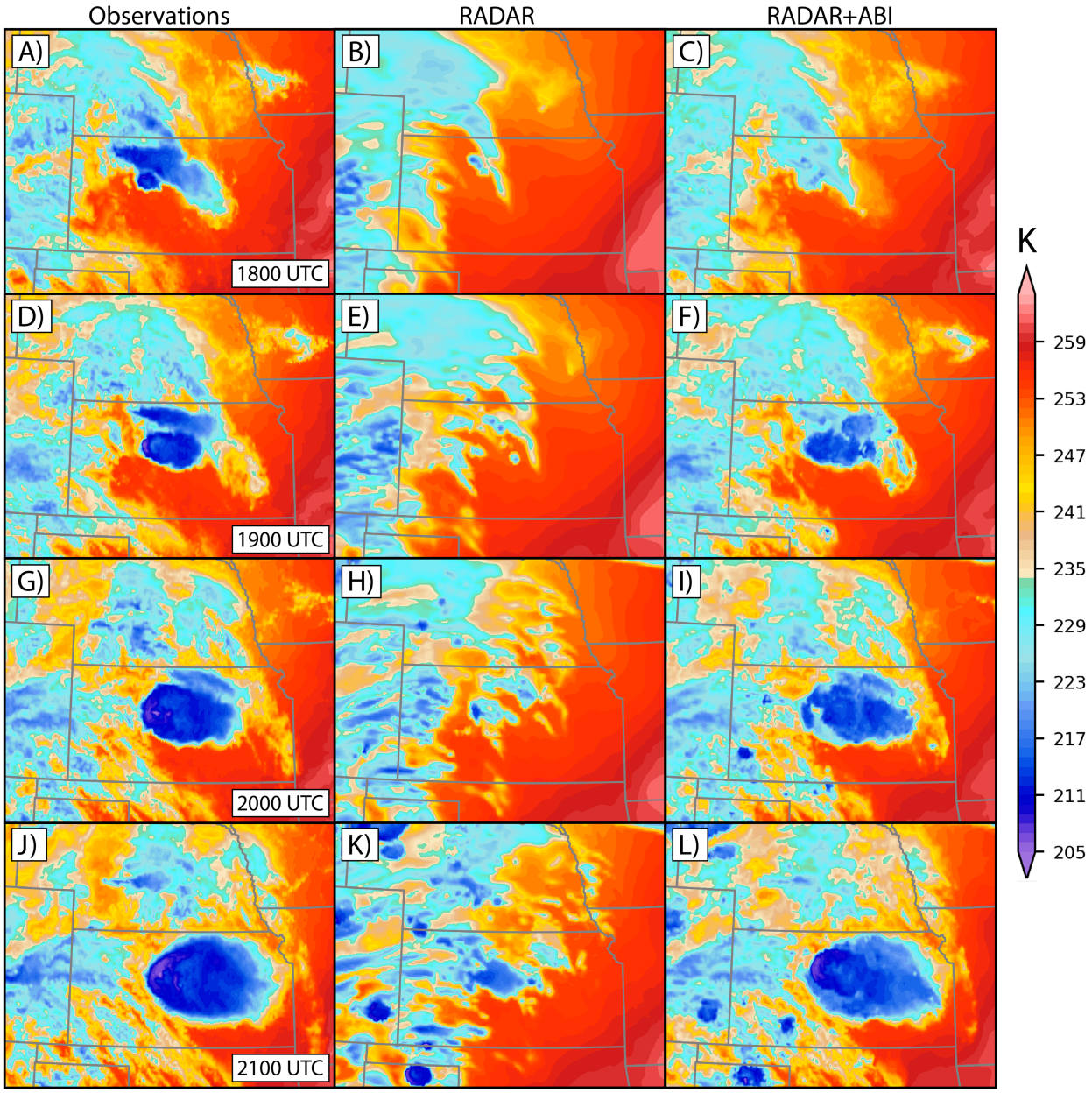

FIG. 10. As in Fig. 9, but for simulated brightness temperature (K).

simulated T_b for spurious clouds are also smaller than those reported in similar studies (e.g., Zhang et al. 2018). We hypothesize that these differences result from an underdispersion of T_b given that each ensemble member simulates spurious clouds in similar regions (i.e., overconvection in FV3-LAM). Although slight shifts in storm location are sufficient to increase the spread and magnitude of increments for reflectivity, such differences do not sufficiently increase the spread for T_b. The spread for T_b remains small given that the anvil clouds occur on greater scales and spread out over a larger region compared to the reflectivity echoes.

c. *Forecast impacts*

Finally, we also examine the impacts when initializing 12-h forecasts from the final analyses of the three observation impact experiments (Figs. 14–16). We focus these results on the convectively active region in Kansas and Nebraska. The reflectivity improvements from assimilating ABI observations continues in the forecast period (Fig. 14a), especially for localized regions of strong convection (Fig. 15). Although the supercell weakens faster than observed when only assimilating radar observations (red circle in Fig. 15b), RADAR+ABI better maintains the decaying storm out to 0300 UTC (Fig. 15c). The better

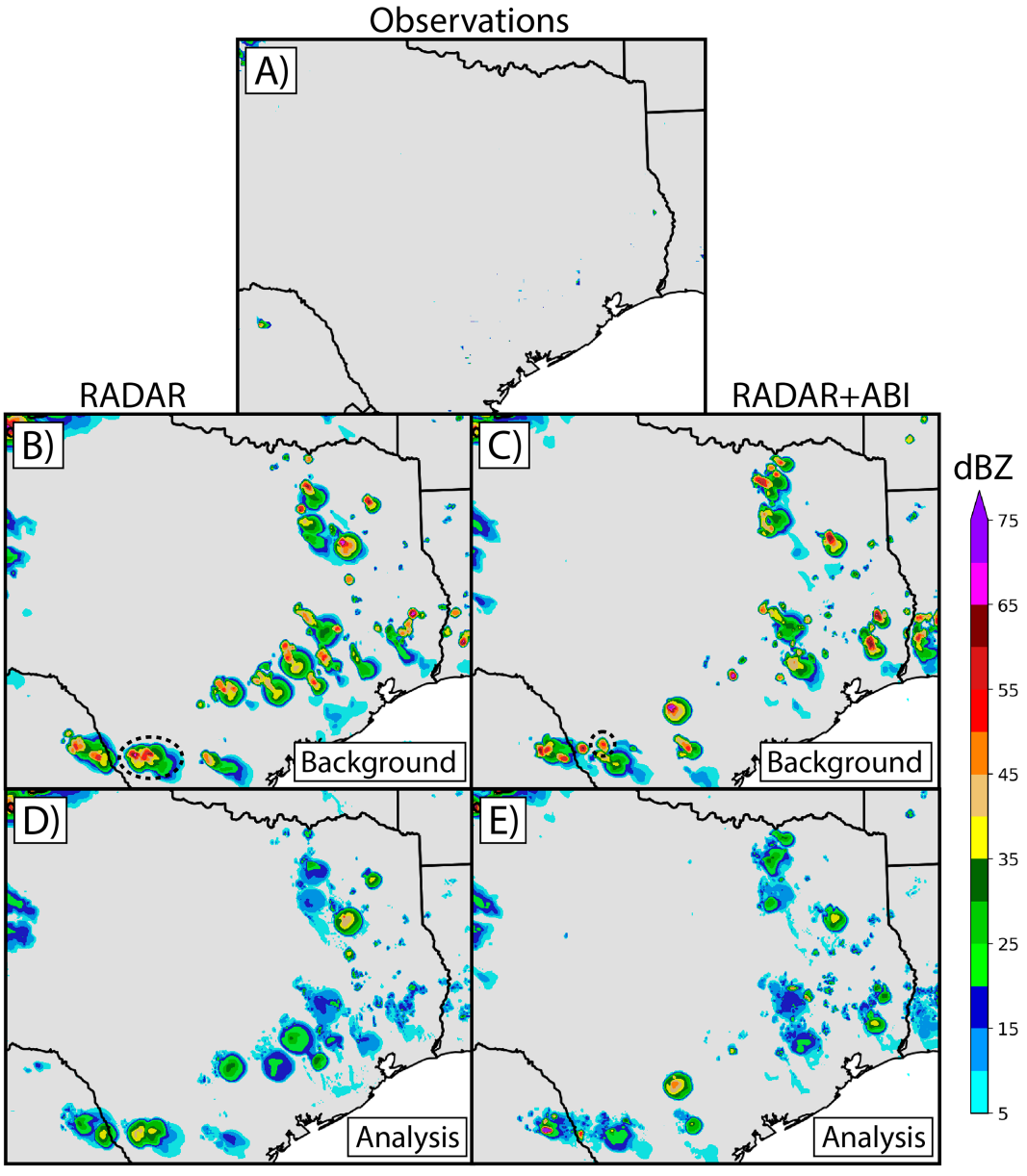

FIG. 11. Composite reflectivity (dBZ) from (a) observations; (b),(c) background; and (d),(e) analysis fields corresponding to spurious convection in eastern Texas during the sixth DA cycle at 2300 UTC 26 May. Shown are background and analysis fields from the (b),(d) RADAR and (c),(e) RADAR+ABI experiment. The circled regions in (b) and (c) indicate the average region used to compute the increment profiles shown in Fig. 13.

forecast for the decaying supercell likely results from the improved analysis and spinup of the anvil cloud that occurs when assimilating ABI radiance observations. RADAR+ABI also better predicts the orientation of the additional convection that develops farther north in Kansas (Fig. 15c), whereas RADAR instead tends to fill in much of this convection at 0300 UTC (Fig. 15b). This convection later develops into a southeastward-propagating MCS by 0700 UTC that is better predicted in both sets of experiments compared to the discrete convection at earlier lead times (Figs. 14a and 15d–f). The MCS is also better predicted in RADAR+ABI (red circle in Fig. 15f) compared to RADAR (red circle in Fig. 15e). These forecast improvements result in moderate but sustained benefits to FSS when computed for reflectivity exceeding 30 dBZ (Fig. 14a), especially during the later half of the forecast when the secondary MCS begins to dominate the verification domain.

Although the T_b impacts were large during the DA cycling, the forecast impacts to the simulated T_b field are nearly neutral when assimilating radiance observations (Fig. 14b). This finding results from the anvil clouds associated with the many convective systems quickly becoming too large and widespread during the forecast period in both experiments (Fig. 16). Given the much

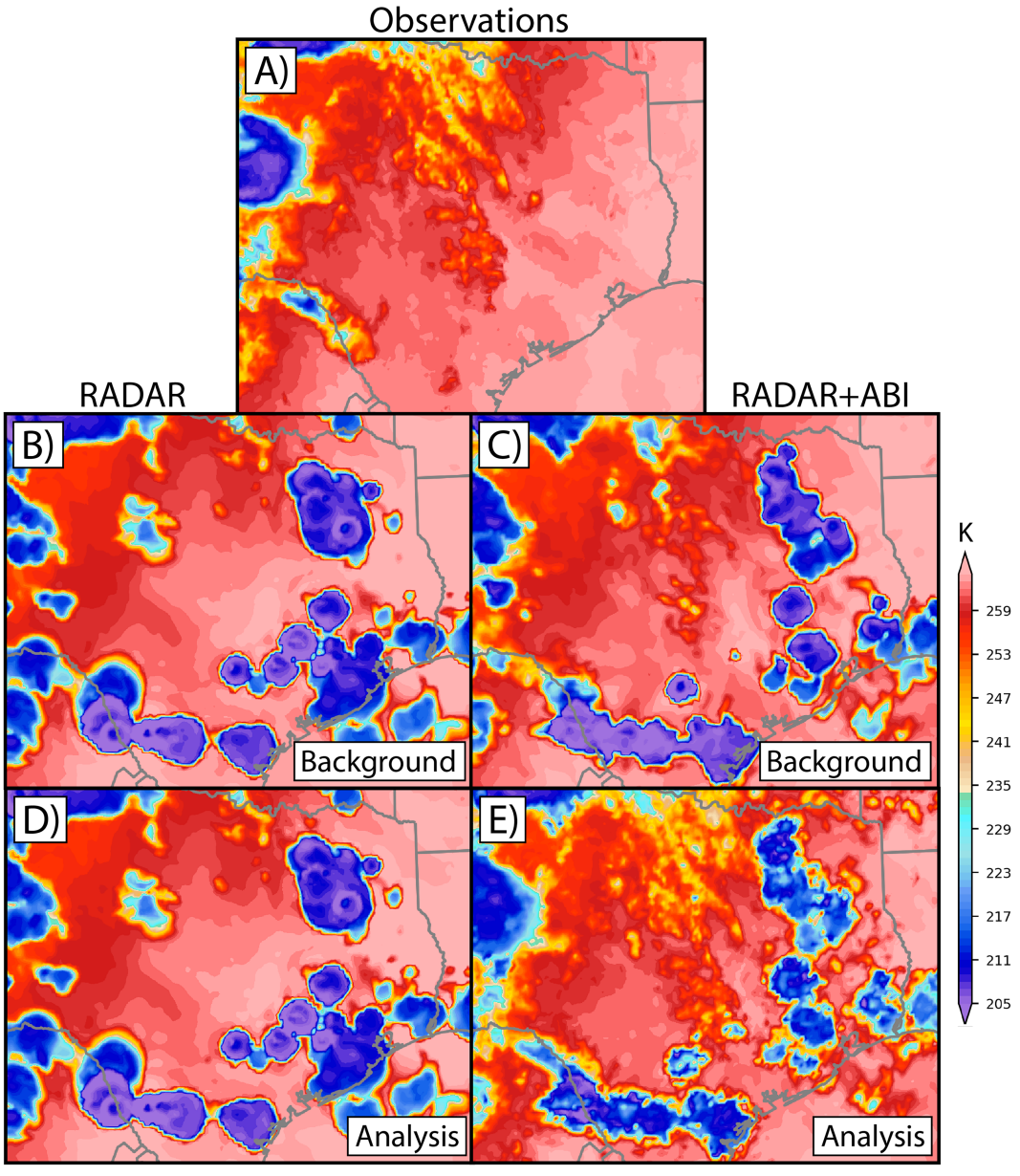

FIG. 12. As in Fig. 11, but for simulated brightness temperature (K).

larger scale associated with the anvil clouds compared to individual reflectivity objects, this overprediction of the anvils masks the smaller-scale benefits discussed earlier for RADAR+ABI. An overprediction of anvil clouds in RRFS is also documented by Johnson et al. (2023). As such, RADAR and RADAR+ABI predict very similar T_b fields, and any benefits from assimilating ABI all-sky radiance observations are only maintained for about the first forecast hour (Fig. 14b).

5. Summary

The ABI aboard *GOES-16* and *GOES-17* provides high-resolution observations of cloud structures that could be highly beneficial for convective-scale DA. However, only the clear-air observations are typically assimilated at operational centers due to a variety of problems associated with cloudy radiance data. As such, many questions remain about how to best assimilate all-sky radiances, especially when using hybrid DA systems such as EnVar wherein a nonlinear observation operator can lead to cost function gradient imbalance and slow minimization. This study explores solutions to this problem by assimilating all-sky radiance observations using a RRFS-like forecast system that features the GSI-based EnVar. RRFS is scheduled to replace the HRRR as the next-generational operational convective forecast system.

We first adjust the RTPS inflation method for RRFS given its tendency to overpredict spurious convection in many parts of the

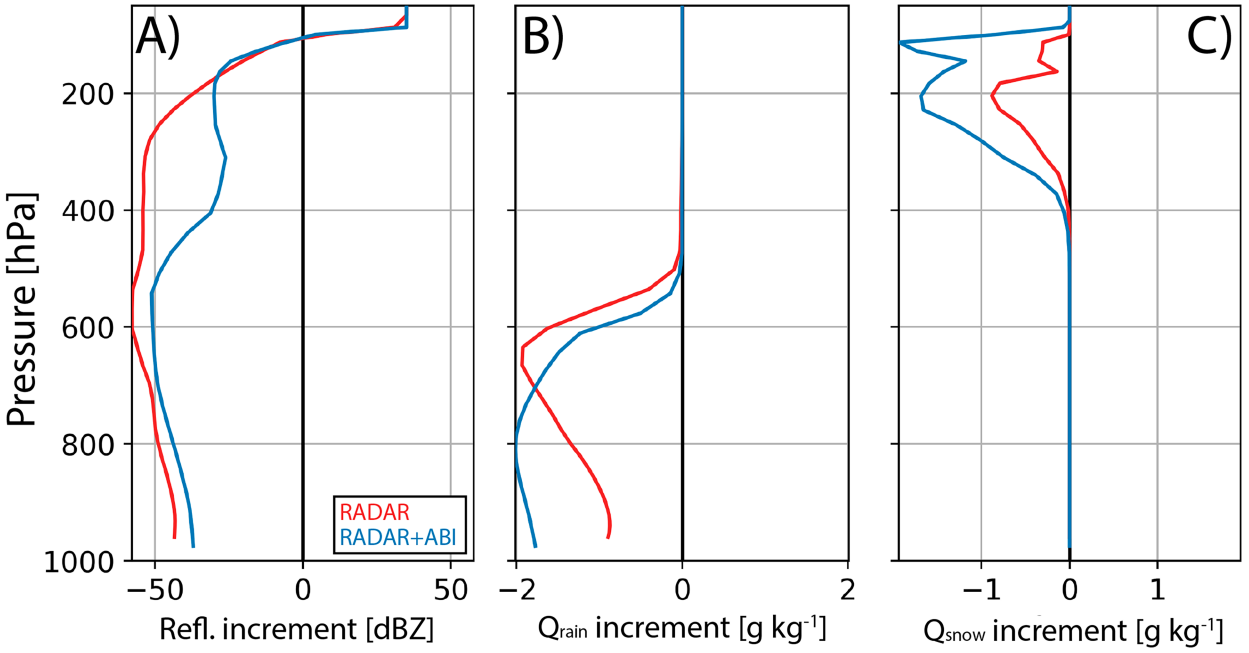

FIG. 13. Increment profiles during the final DA cycle at 0000 UTC 27 May for (a) reflectivity (dBZ), (b) rainwater mixing ratio (g kg^{-1}), and (c) snow mixing ratio (g kg^{-1}). The profiles for RADAR are computed for the grid point at the center of the circle in Fig. 11b, and the profiles for RADAR+ABI are computed for the grid point at the center of the circle in Fig. 11c.

domain. Using standard RTPS inflation parameters in RRFS results in increased spurious convection in the ensemble that would normally be suppressed with a pure EnKF. We find that using a smaller inflation parameter ($\alpha = 0.3$) better suppresses both spurious reflectivity and anvil clouds, leading to large decreases in errors for reflectivity and T_b. Additionally, given the highly nonlinear relationship between brightness temperature and typical state variables, we modify the EnVar solver by directly adding T_b as a state variable. This development reduces the observation operator to an identity matrix and resolves the cost function gradient imbalance. The cost function minimization in EnVar is improved, and observation increments are more realistic and larger. Spurious convection is also further suppressed when including T_b as a state variable.

Assimilating the ABI all-sky radiances using these methods shows large and sustained (~12 h) impacts for forecasts of a

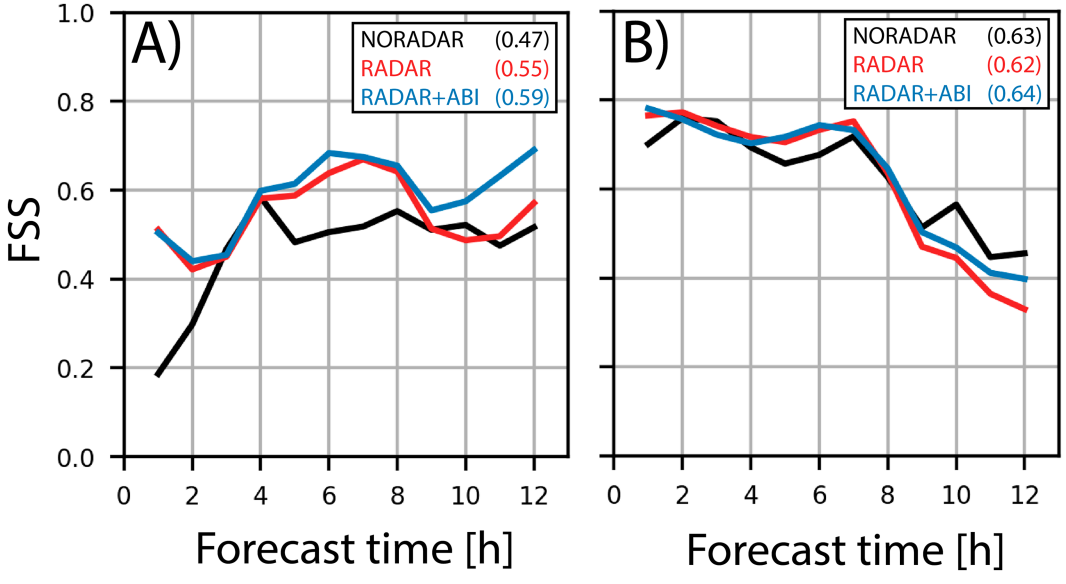

FIG. 14. As in Fig. 6, but for the observation impact experiments.

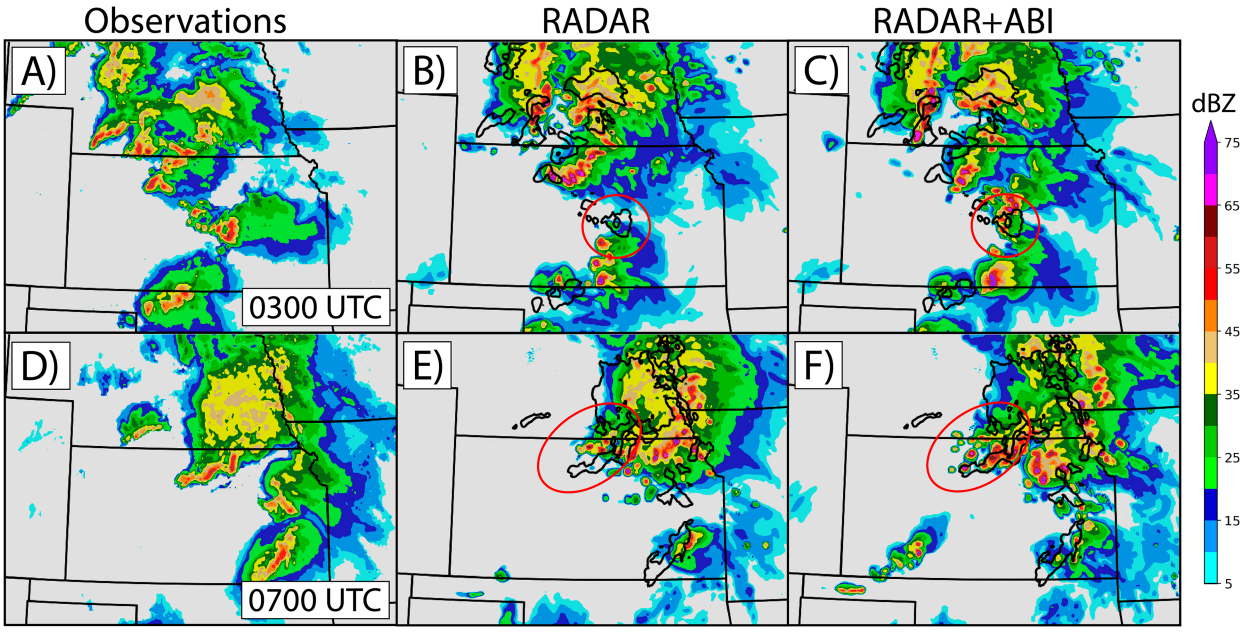

FIG. 15. As in Fig. 9, but valid for the forecast period at (a),(b) 0300 and (c),(d) 0700 UTC 27 May.

severe convective event in central Kansas. We find the ABI observations to be complementary to radar reflectivity observations when suppressing spurious convection. The radar observations remove rain and cloud hydrometeors close to the surface, while assimilating the ABI observations helps suppress ice and snow hydrometeors associated with spurious anvil clouds (i.e., "top-down" suppression). These impacts aid in better analyses of the environment associated with the spurious convection. Additionally, assimilating the ABI observations results in faster spinup of a tornadic supercell. Without assimilating the ABI data, no precipitation or anvil cloud is analyzed until ~3 h after its observed development. These impacts are also maintained throughout the forecast period, as the experiment that assimilates ABI data better predicts the evolution of the original supercell and a later MCS that produced severe wind reports. However, these impacts are primarily constrained to small-scale convective structures. The impacts to cloud structures via T_b quickly erode during the forecast period due to

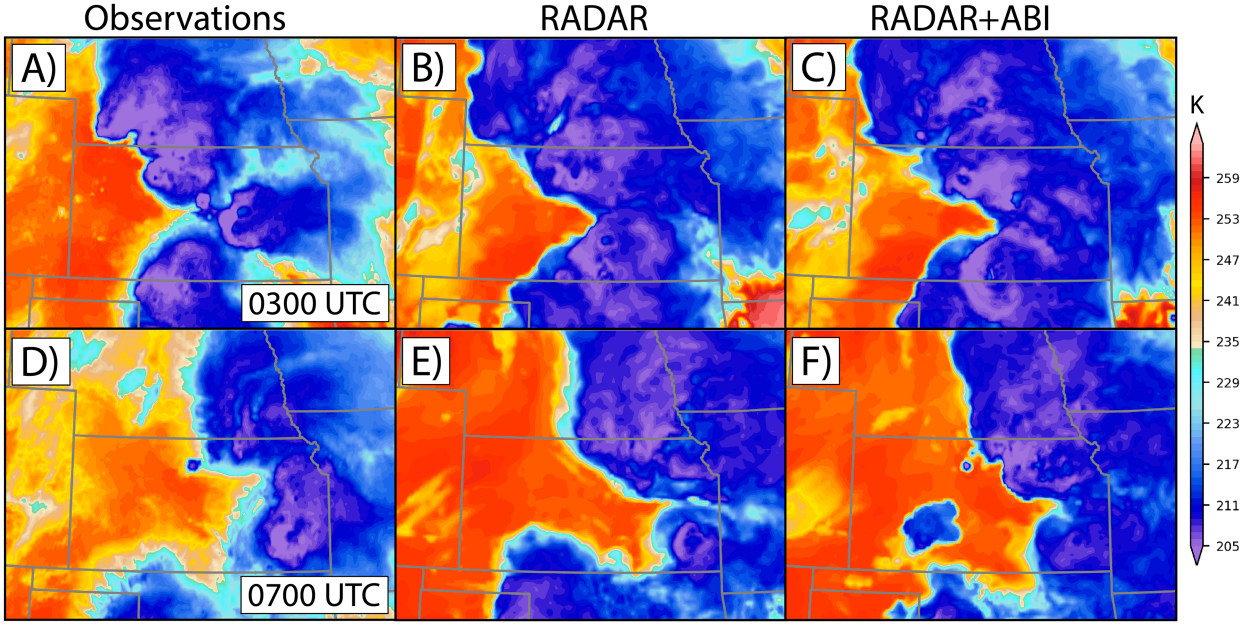

FIG. 16. As in Fig. 10, but valid for the forecast period at (a),(b) 0300 and (c),(d) 0700 UTC 27 May.

model biases that predict too large and widespread of anvil clouds.

Overall, assimilating all-sky radiance observations using an EnVar system can greatly improve analyses and forecasts in convective-scale NWP given that proper methods are used to treat these novel datasets. In the future, we plan to develop static covariances for T_b to fully implement the hybrid approach and improve analysis issues related to underdispersion in the FV3-LAM ensemble. We also plan to compare this EnVar approach with other DA methods and evaluate the impact of the ABI all-sky radiance observations in a multiscale DA context (e.g., Wang et al. 2021; Wang and Wang 2023). Furthermore, we plan to implement techniques to better estimate the observation error statistics for all-sky radiance observations in RRFS using methods developed by Minamide and Zhang (2017) and Johnson et al. (2022). Our initial efforts to employ these methods resulted in large observation errors near convective clouds that greatly reduced the ability for ABI observations to suppress spurious convection. However, future developments of RRFS aim to improve model biases related to this spurious convection. These advancements should lessen the need for ABI observations to resolve the spurious convection problem, thus allowing for larger and more accurate treatment of observation errors. Given the ability for hybrid DA systems to also account for correlated observation errors, employing innovation-based methods such as the Desroziers et al. (2005) technique could even further improve the impacts of assimilating all-sky radiance observations.

Acknowledgments. This project is primarily supported by the NOAA Grant NA16OAR4320115. The authors also wish to acknowledge the Multi-scale data Assimilation and Predictability Laboratory (MAP; http://weather.ou.edu/~map/index.html) at OU.

Data availability statement. All ABI datasets are available online at https://docs.opendata.aws/noaa-goes16/cics-readme.html. Additionally, the model output data for the assimilation experiments are archived locally and available upon request to the corresponding author.

REFERENCES

Aksoy, A., D. C. Dowell, and C. Snyder, 2009: A multicase comparative assessment of the ensemble Kalman filter for assimilation of radar observations. Part I: Storm-scale analyses. *Mon. Wea. Rev.*, **137**, 1805–1824, https://doi.org/10.1175/2008MWR2691.1.

Alexander, C., and J. Carley, 2020: Short-range weather in operations. *UFS Quart.*, Winter 2020, 6–7, NOAA/NWS, Silver Spring, MD, https://repository.library.noaa.gov/view/noaa/30739/noaa_30739_ds1.pdf.

Barker, D., and Coauthors, 2012: The Weather Research and Forecasting Model's Community Variational/Ensemble Data Assimilation System: WRFDA. *Bull. Amer. Meteor. Soc.*, **93**, 831–843, https://doi.org/10.1175/BAMS-D-11-00167.1.

Bathmann, K., and A. Collard, 2020: Surface-dependent correlated infrared observation errors and quality control in the FV3 framework. *Quart. J. Roy. Meteor. Soc.*, **147**, 408–424, https://doi.org/10.1002/qj.3925.

Black, T. L., and Coauthors, 2021: A limited area modeling capability for the finite-volume cubed sphere (FV3) dynamical core and comparison with a global two-way nest. *J. Adv. Model. Earth Syst.*, **13**, e2021MS002483, https://doi.org/10.1029/2021MS002483.

Chandramouli, K., X. Wang, A. Johnson, and J. Otkin, 2022: Online nonlinear bias correction in ensemble Kalman filter to assimilate GOES-R all-sky radiances for the analysis and prediction of rapidly developing supercells. *J. Adv. Model. Earth Syst.*, **14**, e2021MS002711, https://doi.org/10.1029/2021MS002711.

Chen, D., J. Guo, H. Wang, J. Li, M. Min, W. Zhao, and D. Yao, 2018: The cloud top distribution and diurnal variation of clouds over East Asia: Preliminary results from advanced Himawari imager. *J. Geophys. Res. Atmos.*, **123**, 3724–3739, https://doi.org/10.1002/2017JD028044.

Degelia, S. K., X. Wang, D. J. Stensrud, and A. Johnson, 2018: Understanding the impact of radar and in situ observations on the prediction of a nocturnal convection initiation event on 25 June 2013 using an ensemble-based multiscale data assimilation system. *Mon. Wea. Rev.*, **146**, 1837–1859, https://doi.org/10.1175/MWR-D-17-0128.1.

——, ——, ——, and D. D. Turner, 2020: Systematic evaluation of the impact of assimilating a network of ground-based remote sensing profilers for forecasts of nocturnal convection initiation during PECAN. *Mon. Wea. Rev.*, **148**, 4703–4728, https://doi.org/10.1175/MWR-D-20-0118.1.

Derber, J., and A. Rosati, 1989: A global oceanic data assimilation system. *J. Phys. Oceanogr.*, **19**, 1333–1347, https://doi.org/10.1175/1520-0485(1989)019<1333:AGODAS>2.0.CO;2.

Desroziers, G., L. Berre, B. Chapnik, and P. Poli, 2005: Diagnosis of observation, background and analysis-error statistics in observation space. *Quart. J. Roy. Meteor. Soc.*, **131**, 3385–3396, https://doi.org/10.1256/qj.05.108.

Duda, J. D., X. Wang, Y. Wang, and J. R. Carley, 2019: Comparing the assimilation of radar reflectivity using the direct GSI-based ensemble variational (EnVar) and indirect cloud analysis methods in convection-allowing forecasts over the continental United States. *Mon. Wea. Rev.*, **147**, 1655–1678, https://doi.org/10.1175/MWR-D-18-0171.1.

Eure, K. C., P. D. Mykolajtchuk, Y. Zhang, D. J. Stensrud, F. Zhang, S. J. Greybush, and M. R. Kumjian, 2023: Simultaneous assimilation of planetary boundary layer observations from radar and all-sky satellite observations to improve forecasts of convection initiation. *Mon. Wea. Rev.*, **151**, 795–813, https://doi.org/10.1175/MWR-D-22-0188.1.

Gasperoni, N. A., X. Wang, and Y. Wang, 2020: A comparison of methods to sample model errors for convection-allowing ensemble forecasts in the setting of multiscale initial conditions produced by the GSI-based EnVar assimilation system. *Mon. Wea. Rev.*, **148**, 1177–1203, https://doi.org/10.1175/MWR-D-19-0124.1.

——, ——, and ——, 2023: Valid time shifting for an experimental RRFS convection-allowing EnVar data assimilation and forecast system: Description and systematic evaluation in real time. *Mon. Wea. Rev.*, **151**, 1229–1245, https://doi.org/10.1175/MWR-D-22-0089.1.

Han, Y., P. van Delst, Q. Liu, F. Weng, B. Yan, R. Treadon, and J. Derber, 2006: JCSDA Community Radiative Transfer Model (CRTM)—Version 1. NOAA Tech. Rep. NESDIS 122, 33 pp.

Harnisch, F., and C. Keil, 2015: Initial conditions for convective-scale ensemble forecasting provided by ensemble data assimilation.

Mon. Wea. Rev., **143**, 1583–1600, https://doi.org/10.1175/MWR-D-14-00209.1.

Harris, L., X. Chen, W. Putman, L. Zhou, and J.-H. Chen, 2021: A scientific description of the GFDL finite-volume cubed-sphere dynamical core. NOAA Tech. Memo. OAR GFDL 2021-001, 109 pp., https://doi.org/10.25923/6nhs-5897.

Honda, T., and Coauthors, 2018: Assimilating all-sky *Himawari-8* satellite infrared radiances: A case of Typhoon Soudelor (2015). *Mon. Wea. Rev.*, **146**, 213–229, https://doi.org/10.1175/MWR-D-16-0357.1.

Hu, J., N. Yussouf, D. D. Turner, T. A. Jones, and X. Wang, 2019: Impact of ground-based remote sensing boundary layer observations on short-term probabilistic forecasts of a tornadic supercell event. *Wea. Forecasting*, **34**, 1453–1476, https://doi.org/10.1175/WAF-D-18-0200.1.

Iacono, M. J., J. S. Delamere, E. J. Mlawer, M. W. Shephard, S. A. Clough, and W. D. Collins, 2008: Radiative forcing by long-lived greenhouse gases: Calculations with the AER radiative transfer models. *J. Geophys. Res.*, **113**, D13103, https://doi.org/10.1029/2008JD009944.

Johnson, A., X. Wang, and T. Jones, 2022: Impacts of assimilating GOES-16 ABI channels 9 and 10 clear air and cloudy radiance observations with additive inflation and adaptive observation error in GSI-EnKF for a case of rapidly evolving severe supercells. *J. Geophys. Res. Atmos.*, **127**, e2021JD036157, https://doi.org/10.1029/2021JD036157.

——, and Coauthors, 2023: Verification and model configuration sensitivity of simulated ABI radiance forecasts with the FV3-LAM model. *Earth Space Sci.*, **10**, e2022EA002651, https://doi.org/10.1029/2022EA002651.

Jones, T. A., and Coauthors, 2020: Assimilation of *GOES-16* radiances and retrievals into the Warn-on-Forecast System. *Mon. Wea. Rev.*, **148**, 1829–1859, https://doi.org/10.1175/MWR-D-19-0379.1.

Koenig, M., and E. de Coning, 2009: The MSG global instability indices product and its use as a nowcasting tool. *Wea. Forecasting*, **24**, 272–285, https://doi.org/10.1175/2008WAF2222141.1.

Lin, S.-J., 2004: A "vertically Lagrangian" finite-volume dynamical core for global models. *Mon. Wea. Rev.*, **132**, 2293–2307, https://doi.org/10.1175/1520-0493(2004)132<2293:AVLFDC>2.0.CO;2.

Lu, X., X. Wang, Y. Li, and X. Ma, 2017: GSI-based ensemble-variational hybrid data assimilation for HWRF for hurricane initialization and prediction: Impact of various error covariances for airborne radar observation assimilation. *Quart. J. Roy. Meteor. Soc.*, **143**, 223–239, https://doi.org/10.1002/qj.2914.

Minamide, M., and F. Zhang, 2017: Adaptive observation error inflation for assimilating all-sky satellite radiance. *Mon. Wea. Rev.*, **145**, 1063–1081, https://doi.org/10.1175/MWR-D-16-0257.1.

Nakanishi, M., and H. Niino, 2006: An improved Mellor–Yamada level-3 model: Its numerical stability and application to a regional prediction of advection fog. *Bound.-Layer Meteor.*, **119**, 397–407, https://doi.org/10.1007/s10546-005-9030-8.

Oberthaler, A. J., and P. M. Markowski, 2013: A numerical simulation study of the effects of anvil shading on quasi-linear convective systems. *J. Atmos. Sci.*, **70**, 767–793, https://doi.org/10.1175/JAS-D-12-0123.1.

Pan, Y., K. Zhu, M. Xue, X. Wang, M. Hu, S. G. Benjamin, S. S. Weygandt, and J. S. Whitaker, 2014: A GSI-based coupled EnSRF–En3DVar hybrid data assimilation system for the operational Rapid Refresh model: Tests at a reduced resolution. *Mon. Wea. Rev.*, **142**, 3756–3780, https://doi.org/10.1175/MWR-D-13-00242.1.

Putman, W. M., and S.-J. Lin, 2007: Finite-volume transport on various cubed-sphere grids. *J. Comput. Phys.*, **227**, 55–78, https://doi.org/10.1016/j.jcp.2007.07.022.

Roberts, N. M., and H. W. Lean, 2008: Scale-selective verification of rainfall accumulations from high-resolution forecasts of convective events. *Mon. Wea. Rev.*, **136**, 78–97, https://doi.org/10.1175/2007MWR2123.1.

Rogers, E., and Coauthors, 2009: The NCEP North American Mesoscale Modeling System: Recent changes and future plans. *23rd Conf. on Weather Analysis and Forecasting/19th Conf. on Numerical Weather Prediction*, Omaha, NE, Amer. Meteor. Soc., 2A.4, https://ams.confex.com/ams/23WAF19NWP/techprogram/paper_154114.htm.

Saunders, R. W., and K. T. Kriebel, 1988: An improved method for detecting clear sky and cloudy radiances from AVHRR data. *Int. J. Remote Sens.*, **1**, 123–150, https://doi.org/10.1080/01431168808954841.

Schmit, T. J., P. Griffith, M. M. Gunshor, J. M. Daniels, S. J. Goodman, and W. J. Lebair, 2017: A closer look at the ABI on the GOES-R series. *Bull. Amer. Meteor. Soc.*, **98**, 681–698, https://doi.org/10.1175/BAMS-D-15-00230.1.

Smirnova, T. G., J. M. Brown, S. G. Benjamin, and J. S. Kenyon, 2016: Modifications to the Rapid Update Cycle Land Surface Model (RUC LSM) available in the Weather Research and Forecasting (WRF) Model. *Mon. Wea. Rev.*, **144**, 1851–1865, https://doi.org/10.1175/MWR-D-15-0198.1.

Sun, J., and N. A. Crook, 1997: Dynamical and microphysical retrieval from Doppler radar observations using a cloud model and its adjoint. Part I: Model development and simulated data experiments. *J. Atmos. Sci.*, **54**, 1642–1661, https://doi.org/10.1175/1520-0469(1997)054<1642:DAMRFD>2.0.CO;2.

Thompson, G., P. R. Field, R. M. Rasmussen, and W. D. Hall, 2008: Explicit forecasts of winter precipitation using an improved bulk microphysics scheme. Part II: Implementation of a new snow parameterization. *Mon. Wea. Rev.*, **136**, 5095–5115, https://doi.org/10.1175/2008MWR2387.1.

Tong, M., and M. Xue, 2005: Ensemble Kalman filter assimilation of Doppler radar data with a compressible nonhydrostatic model: OSS experiments. *Mon. Wea. Rev.*, **133**, 1789–1807, https://doi.org/10.1175/MWR2898.1.

UFS Development Team, 2022: Unified Forecast System (UFS) Short-Range Weather (SRW) application (version v2.1.0). Zenodo, accessed 1 April 2022, https://doi.org/10.5281/zenodo.7277602.

Wang, C., and X. Huang, 2014: Parallax correction in the analysis of multiple satellite data sets. *IEEE Geosci. Remote Sens. Lett.*, **11**, 965–969, https://doi.org/10.1109/LGRS.2013.2283573.

Wang, X., 2010: Incorporating ensemble covariance in the gridpoint statistical interpolation variational minimization: A mathematical framework. *Mon. Wea. Rev.*, **138**, 2990–2995, https://doi.org/10.1175/2010MWR3245.1.

——, T. M. Hamill, J. S. Whitaker, and C. H. Bishop, 2007: A comparison of hybrid ensemble transform Kalman filter–optimum interpolation and ensemble square root filter analysis schemes. *Mon. Wea. Rev.*, **135**, 1055–1076, https://doi.org/10.1175/MWR3307.1.

——, D. M. Barker, C. Snyder, and T. M. Hamill, 2008a: A hybrid ETKF–3DVAR data assimilation scheme for the WRF Model. Part I: Observing system simulation experiment. *Mon. Wea. Rev.*, **136**, 5116–5131, https://doi.org/10.1175/2008MWR2444.1.

——, ——, ——, and ——, 2008b: A hybrid ETKF–3DVAR data assimilation scheme for the WRF Model. Part II: Real

observation experiments. *Mon. Wea. Rev.*, **136**, 5132–5147, https://doi.org/10.1175/2008MWR2445.1.

——, D. Parrish, D. Kleist, and J. S. Whitaker, 2013: GSI 3DVar-based ensemble–variational hybrid data assimilation for NCEP Global Forecast System: Single-resolution experiments. *Mon. Wea. Rev.*, **141**, 4098–4117, https://doi.org/10.1175/MWR-D-12-00141.1.

——, H. G. Chipilski, C. H. Bishop, E. Satterfield, N. Baker, and J. S. Whitaker, 2021: A multiscale local gain form ensemble transform Kalman filter (MLGETKF). *Mon. Wea. Rev.*, **149**, 605–622, https://doi.org/10.1175/MWR-D-20-0290.1.

Wang, Y., and X. Wang, 2017: Direct assimilation of radar reflectivity without tangent linear and adjoint of the nonlinear observation operator in the GSI-Based EnVar System: Methodology and experiment with the 8 May 2003 Oklahoma City tornadic supercell. *Mon. Wea. Rev.*, **145**, 1447–1471, https://doi.org/10.1175/MWR-D-16-0231.1.

——, and ——, 2021a: Development of convective-scale static background error covariance within GSI-based hybrid EnVar system for direct radar reflectivity data assimilation. *Mon. Wea. Rev.*, **149**, 2713–2736, https://doi.org/10.1175/MWR-D-20-0215.1.

——, and ——, 2021b: Rapid update with EnVar direct radar reflectivity data assimilation for the NOAA regional convection-allowing NMMB model over the CONUS: System description and initial experiment results. *Atmosphere*, **12**, 1286, https://doi.org/10.3390/atmos12101286.

——, and ——, 2023: Simultaneous multiscale data assimilation using scale- and variable-dependent localization in EnVar for convection allowing analyses and forecasts: Methodology and experiments for a tornadic supercell. *J. Adv. Model. Earth Syst.*, **15**, e2022MS003430, https://doi.org/10.1029/2022MS003430.

——, Y. Chen, and J. Min, 2022: Improving the prediction of heavy rainfall with rapid-update dual-resolution hybrid En3DVar assimilation of all-sky AHI infrared water vapor radiances. *Atmos. Res.*, **279**, 106352, https://doi.org/10.1016/j.atmosres.2022.106352.

Wei, M., Z. Toth, R. Wobus, and Y. Zhu, 2008: Initial perturbations based on the ensemble transform (ET) technique in the NCEP global operational forecast system. *Tellus*, **60A**, 62–79, https://doi.org/10.1111/j.1600-0870.2007.00273.x.

Weston, P. P., W. Bell, and J. R. Eyre, 2014: Accounting for correlated error in the assimilation of high-resolution sounder data. *Quart. J. Roy. Meteor. Soc.*, **140**, 2420–2429, https://doi.org/10.1002/qj.2306.

Whitaker, J. S., and T. M. Hamill, 2002: Ensemble data assimilation without perturbed observations. *Mon. Wea. Rev.*, **130**, 1913–1924, https://doi.org/10.1175/1520-0493(2002)130<1913:EDAWPO>2.0.CO;2.

——, and ——, 2012: Evaluating methods to account for system errors in ensemble data assimilation. *Mon. Wea. Rev.*, **140**, 3078–3089, https://doi.org/10.1175/MWR-D-11-00276.1.

Wicker, L., L. Reames, and T. Mansell, 2020: Simulations of convection using the FV3 SAR in homogeneous environments. *UFS Workshop*, Norman OK, NOAA/National Severe Storms Lab, 19 pp., https://dtcenter.org/sites/default/files/events/2020/1-wicker-lou-1.pdf.

Wu, W.-S., J. R. Purser, and D. F. Parrish, 2002: Three-dimensional variational analysis with spatially inhomogeneous covariances. *Mon. Wea. Rev.*, **130**, 2905–2916, https://doi.org/10.1175/1520-0493(2002)130<2905:TDVAWS>2.0.CO;2.

Yang, Y., and X. Wang, 2023: Impact of radar reflectivity assimilation frequency on convection-allowing forecasts of diverse cases over the continental United States. *Mon. Wea. Rev.*, **151**, 341–362, https://doi.org/10.1175/MWR-D-22-0095.1.

Zhang, J., and Coauthors, 2016: Multi-Radar Multi-Sensor (MRMS) quantitative precipitation estimation: Initial operating capabilities. *Bull. Amer. Meteor. Soc.*, **97**, 621–638, https://doi.org/10.1175/BAMS-D-14-00174.1.

Zhang, Y., F. Zhang, and D. J. Stensrud, 2018: Assimilating all-sky infrared radiances from *GOES-16* ABI using an ensemble Kalman filter for convection-allowing severe thunderstorms prediction. *Mon. Wea. Rev.*, **146**, 3363–3381, https://doi.org/10.1175/MWR-D-18-0062.1.

——, D. J. Stensrud, and F. Zhang, 2019: Simultaneous assimilation of radar and all-sky satellite infrared radiance observations for convection-allowing ensemble analysis and prediction of severe thunderstorms. *Mon. Wea. Rev.*, **147**, 4389–4409, https://doi.org/10.1175/MWR-D-19-0163.1.

——, ——, and E. E. Clothiaux, 2021: Benefits of the Advanced Baseline Imager (ABI) for ensemble-based analysis and prediction of severe thunderstorms. *Mon. Wea. Rev.*, **149**, 313–332, https://doi.org/10.1175/MWR-D-20-0254.1.

Zhu, L., M. Xue, R. Kong, and J. Mind, 2023: Direct assimilation of all-sky GOES-R ABI radiances in GSI EnKF for the analysis and forecasting of a mesoscale convective system. *Mon. Wea. Rev.*, **151**, 737–760, https://doi.org/10.1175/MWR-D-21-0293.1.